**Title**
Role of atmospheric dust in controlling Earth's riverine silicate weathering flux



**Author**
Plante, Zachary T

**Publication Date**
2022

Peer reviewed|Thesis/dissertation

UNIVERSITY OF CALIFORNIA

Los Angeles

# Role of atmospheric dust in controlling Earth's riverine silicate weathering flux

A thesis submitted in partial satisfaction of the

requirements for the degree Master of Science

in Geology

by

Zachary Thomas Elias Plante

2022

ABSTRACT OF THE THESIS

Role of atmospheric dust in controlling Earth's riverine silicate weathering flux

by

Zachary Thomas Elias Plante

Master of Science in Geology

University of California, Los Angeles, 2022

Professor Seul Gi Moon, Chair

Chemical weathering of bedrock plays a central role in regulating Earth's biogeochemical cycles and atmospheric $CO_2$. However, how dust weathering rates contribute to the total weathering budget remains poorly known. Here, we address this question by testing a hypothesis that continental weathering of dust could possibly account for a substantial proportion of the total silicate weathering budget estimated from dissolved chemical loads in rivers. To accomplish this, we calculated a mass balance of atmospheric general-circulation-model estimates of dust deposition (elemental inputs to the land surface) and measurements of riverine dissolved load (elemental outputs) for 44 rivers from around the globe. We first estimated an upper bound of dust contribution to total weathering. Then, we used a steady-state weathering model of shallow weathering to estimate the proportions of dust and rock weathering. Our results show that the magnitude and spatial distribution of dust deposition can

account for a substantial amount of silicate-derived measured dissolved chemical flux in rivers. The predicted fractions of Si and silicate-derived Ca + Mg flux that are produced by dust weathering are both independently 41%, which represent substantial components of total Si and silicate-derived Ca + Mg weathering fluxes. According to these weathering proportions, rock and dust contributions could be similar during both modern and Last Glacial Maximum periods. While our results do not rule out the long-held view that rock weathering in soil dominates continental weathering fluxes, they also do not rule out a scenario in which dust accounts for a substantial fraction of observed global dissolved loads. Our results also highlight the need to better understand the dynamics of dust deposition and subsequent weathering when assessing regional and global weathering impacts on biogeochemical cycling and long-term climate change.

The thesis of Zachary Thomas Elias Plante is approved.

An Yin

Gilles F. Peltzer

Seul Gi Moon, Committee Chair

University of California, Los Angeles

2022

# Table of Contents

LIST OF FIGURES page

LIST OF SUPPLEMENTARY MATERIALS page

ACKNOWLEDGEMENTS

We would like to thank Ken Ferrier and one anonymous reviewer for constructive reviews and Andrew Jacobson for editorial support. This work was supported by the National Science Foundation [grant numbers 19–45431, 20–12073]. This work is in preparation for publication.

AUTHOR LIST AND CONTRIBUTIONS

- Zach Plante: Conceptualization, Methodology, Formal analysis, Investigation, Data Curation, Writing - Original Draft, Writing - Review & Editing, Visualization
- George Hilley: Conceptualization, Methodology, Software, Formal analysis, Investigation, Writing - Review & Editing, Supervision, Project administration
- Seulgi Moon: Conceptualization, Methodology, Software, Formal analysis, Investigation, Writing - Review & Editing, Supervision, Project administration
- Nathan Brown: Investigation, Writing - Review & Editing
- Julie Fosdick: Investigation, Writing - Review & Editing

# 1. Introduction

Chemical weathering of geologic materials plays a central role in regulating Earth's biogeochemical cycles (Kurtz et al., 2001; Aciego et al., 2017; Arvin et al., 2017), and potentially the drawdown of atmospheric $CO_2$ on geologic timescales (Raymo and Ruddiman, 1992; Hilley and Porder, 2008; Torres et al., 2017). Differences between geologic materials such as dust and bedrock lead to differing contributions of weathering products to the Earth system at different rates (Hilley and Porder, 2008; Macdonald et al., 2019; Mahowald et al., 2005; Ridgwell and Kohfeld, 2002). One view of how geologic materials enter biogeochemical systems is through the chemical modification of bedrock as it weathers to soil. In this case, the rates at which bedrock is delivered to the weathering zone may impact the rate at which rock is weathered to soil (Ferrier et al., 2016; Hilley et al., 2010; Riebe et al., 2004). It is the chemical conversion of rock to soil in the weathering zone that releases chemical elements into global biogeochemical systems.

However, there are non-bedrock sources that may be substantial inputs to the weathering process. For example, portions of Earth have seen high levels of atmospheric dust deposition, often transported from areas thousands of kilometers away both now and in the recent past (Mahowald et al., 2006). According to global dust transport models (e.g., Tanaka and Chiba, 2006), the majority of present-day dust comes from desert regions in North Africa and China. This implies that, if the airborne materials were redistributed from dry to wet areas and chemically weathered once deposited, they might constitute an appreciable input to global

weathering budgets and biogeochemical cycles. Dust generally has a far smaller particle size, and thus greater reactive surface area, than bedrock fragments in the weathering zone (Hilley and Porder, 2008; Marcotte et al., 2020; Simonson, 1995). Dust has been demonstrated to be a significant constituent of soils and geochemical inputs to ecosystems in places such as Hawai'i according to soil mineralogy and isotope geochemistry (Kurtz et al., 2001). In addition, previous studies have suggested that nutrient supply to forest ecosystems may be dominated by dust inputs over those of bedrock in highly weathered soils from tropical to non-tropical montane forests (Porder et al., 2006; Pett-Ridge et al., 2009; Aciego et al., 2017).

These findings raise the possibility that chemical inputs to biogeochemical cycles could be strongly influenced by the production, transport, and weathering of this fine material (Aciego et al., 2017; Mahowald et al., 2005; Ridgwell and Kohfeld, 2002; Ridgwell and Watson, 2002). Tracking this contribution is typically difficult because atmospheric dust and average upper continental crust (UCC) are often chemically and mineralogically similar (Lawrence and Neff, 2009; Taylor and McLennan, 1985). Especially in large catchments whose source rock compositions are close to the average UCC, distinguishing between *in situ* rock weathering and dust weathering is difficult. In addition, the products of chemical weathering of dust are transported away from the weathering zone through dissolved load in rivers. For this reason, the role of atmospheric (global) and other coarser (local and regional) dust is often acknowledged but generally neglected in mineral weathering and biogeochemical studies (Dixon et al., 2009; Ferrier et al., 2016; Riebe et al., 2004). Some locations show evidence for substantial enrichment/depletion of certain elements in dust relative to average UCC (Aarons et

al., 2019; Aciego et al., 2017; Lawrence and Neff, 2009). However, a paucity of long-term measurements of atmospheric dust composition prevents adequate global constraint on composition and degree of mixing. Furthermore, limited studies have been conducted to constrain the relative contributions from rock and dust weathering and their contributions to dissolved loads in rivers.

In this contribution, we utilize a mass balance model to assess whether atmospheric dust could potentially be a substantial contributor to global silicate weathering rates estimated from riverine dissolved loads. To do this, we first estimate an upper bound of dust contribution to total rock and dust weathering by comparing atmospheric GCM-estimates of dust surface deposition and measurements of riverine dissolved load (elemental outputs) for rivers. We then apply a steady-state weathering model of dust and rock weathering within the shallow subsurface weathering zone, including soil and saprolite, to estimate the dust and rock silicate weathering fluxes. Our work shows that a substantial amount of total Si and silicate-derived Ca + Mg (hereinafter, SCM) weathering fluxes might be derived from dust weathering. Our work highlights the potential importance of dust contribution to the global silicate weathering budget and global climate-weathering feedbacks.

# 2. Mass balance of atmospheric dust deposition and riverine flux

We first performed a global analysis that quantifies the accumulation of elements introduced by dust deposition and the flux of elements exiting landscapes by riverine dissolved load (RDL). In doing this, we assessed whether weathering of atmospheric dust could possibly explain the magnitude and distribution of measured RDL flux of Si and SCM across Earth's surface. We used general circulation model (GCM)-derived estimates of modern dust deposition (mass flux, g $m^{-2}$ $yr^{-1}$) from Mahowald et al. (2006) at 0.5° resolution with global coverage. We projected and interpolated these mass fluxes to a 1 $km^2$ grid, whose grid cell locations matched those reported by the Earth Resources Observation and Science (EROS) Center's Hydro1K dataset (Lehner et al., 2008). We then calculated the total modern rate of dust deposition in 44 watersheds for which RDL fluxes from silicate weathering separated from other sources exist (G.E.M.S./Water, 2011; H.Y.B.A.M., 2013; Moon et al., 2014), as well as the total dust deposition rate (g $yr^{-1}$) by integrating dust-derived mass deposition over each watershed area (Table 1). We converted each deposition rate into an elemental discharge for each catchment (mol $yr^{-1}$) by assuming atmospheric dust is compositionally identical to average UCC (Hren et al., 2007; Rudnick and Gao, 2013; White and Brantley, 2003) (Table 2).

We compared these dust-derived elemental discharges to observed dissolved chemical discharges in 44 rivers. We considered riverine discharges of Si from 22 basins SCM from 35 basins where adequate chemistry and water runoff data exist in the Global Environment

Monitoring System for freshwater (GEMS) dataset (G.E.M.S./Water, 2011). We calculated time-averaged riverine ion discharges ($r_j$, mol $yr^{-1}$) for each basin based on previous measurements (Moon et al., 2014). These values were calculated using a time-series of contemporaneous ion concentration and water runoff measurements to calculate the ensemble mean of these quantities. Where data were sampled too sparsely in time to perform this averaging, we used the product of the averaged measured cation concentration and flux to calculate elemental discharges (Moon et al., 2014). Si discharge (mol $yr^{-1}$) is considered because Si is the most prevalent cation found in bedrock and dust. The proportion of SCM is quantified based on mass balance equations of Na-normalized elemental ratios assuming four endmembers of chemical sources (e.g., atmospheric input as sea salt, evaporite, carbonate, and silicate) (Gaillardet et al., 1999; Moon et al., 2014). SCM discharges further allow us to compare the dust contribution to mineral weathering of potentially different reactive mineral phases of silicates.

Then, we compared the potential elemental discharges from dust deposition and the measured elemental discharges from riverine fluxes of Si and SCM. We calculated $\delta_j^*$, an upper bound for the proportion of RDL discharges that could be explained by dust input, where $j$ represents the given solute ion phase (Si or SCM). $\delta_j^*$ is equivalent to dust deposition (mol $yr^{-1}$) divided by RDL discharge (mol $yr^{-1}$) for each solute phase sampled (Si and SCM). Where dust deposition rates exceeded RDL discharges, we set this fraction equal to unity ($\delta_j^* = 1$). This is because an excess of dust deposition cannot further explain RDL discharge. A ratio of fluxes (mol $m^{-2}$ $yr^{-1}$) can also be used due to a lack of basin area dependence in $\delta_j^*$.

The results for our mass balance analysis indicate that the upper bounds of potential dust contribution to riverine weathering fluxes can be appreciable in these rivers (Figure 1). Measured elemental discharges range from $4.73\times10^{7}$ – $4.18\times10^{11}$ mol $yr^{-1}$ for Si and $3.65\times10^{7}$ – $1.90\times10^{11}$ mol $yr^{-1}$ for SCM. When calculating dust inputs to these watersheds, we find elemental deposition ranges (mol $yr^{-1}$) of $2.18\times10^{8}$ – $9.94\times10^{11}$ for Si and $2.47\times10^{7}$ – $1.13\times10^{11}$ for SCM, assuming that dust is entirely silicate-derived. Among all sampled rivers, 15 out of 22 watersheds show an excess of dust-derived Si relative to that recorded in the solute load ($\delta_{Si}$*= 1). For SCM, 9 out of 35 watersheds have $\delta_{SCM}$*= 1 (Figure 1). The average $\delta_{Si}$*and $\delta_{SCM}$* are 0.87 and 0.47, respectively.

The central assumptions underpinning our analysis are: 1) there is no substantial storage or release of dust in surface soils or groundwater that would account for differences between dust inputs and dust-derived solute outputs in rivers, and 2) all dust that enters soil weathers to completion. When both conditions are met, the actual $\delta_j$* will equal the calculated $\delta_j$*. Clearly, these assumptions may not be valid in real landscapes. Due to the dust input flux, material turnover time, and weathering reaction kinetics, dust materials may not be weathered to completion in many places. In fact, loess deposits are often found in eroding or non-eroding landscapes (e.g., the Mississippi Basin, Alaska, and the Sahara) (Goddéris et al., 2010; Roberts et al., 2003). Thus, our calculated $\delta_j$* is likely an upper bound of the actual $\delta_j$*.

# 3. Steady-state model of rock and dust weathering within the subsurface weathering zone

To relax central assumptions 1) and 2) and to estimate more accurate dust contribution to weathering fluxes, we need to quantify weathering fluxes from both rock and dust sources within the subsurface weathering zone, considering the possibility that weathering of rock and dust have not proceeded to completion. To do this, we use a steady-state model of rock and dust weathering to estimate Si and SCM fluxes from rock and dust weathering in rivers for modern dust deposition rates and residence times.

In our model, we account for the weathering of two material phases (rock and dust) in two layers (saprolite and soil) where weathering takes place in the subsurface (Figure 3). We assume that fresh bedrock is moved into the saprolite and then soil by surface erosion and soil production. In the soil, weathered bedrock from saprolite is mixed with, and weathers further alongside, atmospheric dust. Our approach implicitly assumes that weathering occurs within the saprolite and soil, rather than in other depositional areas of landscapes, such as floodplains. For simplicity, we assume that a simple steady-state model of weathering takes place in the entire study area. We determined the total contribution to the observed solute flux of (1) rock weathering within the saprolite zone (where it is unmixed), (2) rock weathering in the mobile soil (where it is mixed), and (3) dust weathering as it is mixed throughout the soil.

Our weathering model assumes that the rate of weathering is a function of both mineral supply and reaction kinetics (Ferrier and Kirchner, 2008; Hilley et al., 2010; Waldbauer and Chamberlain, 2005). We may write the conservation of mass for a particular mineral phase $i$ in weathering zone as:

$$\frac{dN_i}{dt} + \frac{d(\varepsilon N_i)}{dz} = P_i \tag{1}$$

where $N_i$ is the concentration (mol m$^{-3}$) of a particular mineral phase $i$ (i.e., quartz (qz), non-quartz silicate minerals (nqz)), $\varepsilon$ is the erosion rate (m yr$^{-1}$) that moves material from the bottom of the weathering zone toward the surface, $z$ is the distance (m) from the bottom of the weathering zone, and $P_i$ is the volumetric rate of mineral phase $i$ addition or removal (mol m$^{-3}$ yr$^{-1}$) as a source or sink term. For instance, this term can account for processes such as the assimilation of dust into the weathering zone or the removal of materials through chemical weathering or physical erosion. We assume that the weathering profile has reached a steady-state condition. In this case, the weathering profiles (e.g., concentration, thickness) do not change over time (e.g., $\frac{dN_i}{dt} = 0$). The supply rate of fresh minerals to the weathering zone is coupled to the rate at which erosion removes material from the surface. For simplicity, we assume a linear reaction rate law for chemical weathering for a one-dimensional eroding weathering profile. In this case, the weathering rate of fresh minerals is a function of the concentration $N_i$ (mol m$^{-3}$) and reaction rate ($K_i$, yr$^{-1}$). $K_i$ is related to the kinetic constant of the reaction $k_i$ (m$^{-2}$ yr$^{-1}$) and the reactive surface area ($S_i$ , m$^2$) as:

$$K_i = k_i S_i \tag{2}$$

We further assume for simplicity that $k_i$ and $S_i$ do not change with time, and that rock and dust have the same $k_i$ but different $S_i$. Dust's higher $S_i$ requires different values of $K_i$ (hereafter, ${}^{b}K_i$ for material phase $b$ (i.e., rock or dust)).

The volume rate of solute production ($B_{j,i}$, mol m$^{-3}$ yr$^{-1}$) for a particular ion $j$ (i.e., Si, silicate-derived Ca + Mg (SCM)) from a particular mineral phase $i$ is:

$$B_{j,i} = R_{j,i} K_i N_i \tag{3}$$

where $R_{j,i}$ is the stoichiometric ratio between the reacting mineral phase $i$ and the produced solute $j$. We then integrate $B_{j,i}$ over the weathering layer $a$ for material $b$ to produce the solute flux (${}^{a,b}F_{j,i}$, mol m$^{-2}$ yr$^{-1}$) of a given solute ion $j$ from mineral phase $i$ as:

$${}^{a,b}F_{j,i} = \int_{z_b}^{z_u} {}^{a,b}B_{j,i}\, dz \tag{4}$$

where $z_b$ and $z_u$ refers to bottom and upper boundary position (m) of layer $a$, respectively. Then, we sum the solute rates from all mineral phases to produce the total solute flux (${}^{a,b}F_j$, mol m$^{-2}$ yr$^{-1}$) as:

$${}^{a,b}F_j = \sum_i {}^{a,b}F_{j,i} \tag{5}$$

We assume that the soil is well-mixed while the saprolite is not, no dust weathering occurs in the saprolite, and rock fragments entering the soil may have undergone some degree of

weathering in the saprolite. Thus, chemical weathering shown in eq. (1) are specified separately for saprolite and soil as described below.

For the case of saprolite, we assume that fresh bedrock moves through saprolite at a velocity equal to the erosion rate $\varepsilon$ and undergoes chemical reaction. In this case, eq. (1) for the steady-state weathering of saprolite can be as:

$$\varepsilon \frac{d^{sap,rock}N_i}{dz} = -^{rock}K_i \, ^{sap,rock}N_i \tag{6}$$

Solving for $^{sap,rock}N_i$, applying eqs. (3) and (4), and requiring that $^{sap,rock}F_j = 0$ when $^{sap}h = 0$ ($^{sap}h$ is the total thickness of the saprolite (m)), yields a solute flux of a given ion $j$ produced by rock weathering in the saprolite zone ($^{sap,rock}F_j$, mol m$^{-2}$ yr$^{-1}$) of:

$$^{sap,rock}F_j = \sum_i R_{j,i} N_{i,0} \varepsilon \left[1 - e^{-\frac{^{rock}K_i \, ^{sap}h}{\varepsilon}}\right] \tag{7}$$

where $N_{i,0}$ is the concentration of the particular mineral phase $i$ in the unweathered, fresh bedrock (mol m$^{-3}$) (Appendix A).

Next, we consider the amount of rock and dust weathering that occurs within the soil. In this case, saprolite is added to the base of the soil and dust is added to the top of the soil. The actual modes of rock and dust advection into the soil differ, as rock is advected upward from saprolite and dust is advected downward via deposition. We assume both materials are mixed

through the entirety of the soil, such that $\frac{dN_i}{dz} = 0$. The concentration of phase $i$ in soil changes due to chemical weathering and physical erosion of material from the top of the soil.

For rock weathering in the soil that accounts for the rate of phase addition from saprolite, erosional removal, and chemical reaction, eq. (1) is written as:

$$\frac{\varepsilon}{{}^{soil}h}\left(N_i(z_s) - {}^{soil,rock}N_i\right) - K_i\,{}^{soil,rock}N_i = 0 \tag{8}$$

where ${}^{soil}h$ is the total thickness of the soil (m) and $N_i(z_s)$ is equivalent to $N_{i,0}e^{-\frac{{}^{rock}K_i\,{}^{sap}h}{\varepsilon}}$, representing the concentration of weathered rock added to the base of soil ($z_s$). In this case, the solute flux of a given ion *j* from rock weathering in the soil (${}^{soil,rock}F_j$, mol m$^{-2}$ yr$^{-1}$) is:

$${}^{soil,rock}F_j = \sum_i \frac{R_{j,i}N_{i,0}\varepsilon\,{}^{rock}K_i\,{}^{soil}h\,e^{-\frac{{}^{rock}K_i\,{}^{sap}h}{\varepsilon}}}{{}^{rock}K_i\,{}^{soil}h + \varepsilon} \tag{9}$$

Together, this produces a total solute flux from rock weathering within soil and saprolite as:

$${}^{total,rock}F_j = \sum_i R_{j,i}N_{i,0}\varepsilon\left[1 - \frac{\varepsilon\,e^{-\frac{{}^{rock}K_i\,{}^{soil}h\,z^*}{\varepsilon}}}{{}^{rock}K_i\,{}^{soil}h + \varepsilon}\right] \tag{10}$$

where $z^* = \frac{{}^{sap}h}{{}^{soil}h}$.

Finally, we assimilate dust into the soil and allow it to weather within the soil. The reaction rate for dust ($^{dust}K_i$ , yr$^{-1}$) is calculated using the $S_i$ of dust and the kinetic reaction constant $k_i$ that is the same as that of rock material. The larger $S_i$ of dust implies a larger $^{dust}K_i$, which accounts for the fact that dust might weather more rapidly than rock within the soil. Accounting for the rate of phase addition, erosional removal, and chemical reaction of dust material, for eq. (1) is written as:

$$\frac{D_i}{{}_{soil}h} - \frac{\varepsilon^{soil,dust}N_i}{{}_{soil}h} - K_i\ {}^{soil,dust}N_i = 0 \tag{11}$$

where $D_i$ is the dust flux (mol m$^{-2}$ yr$^{-1}$) of the mineral phase $i$. When repeating the above process, we formulate the solute $j$ flux due to dust weathering in the soil ($^{soil,dust}F_j$, mol m$^{-2}$ yr$^{-1}$) as:

$${}^{soil,dust}F_j = \sum_i \frac{R_{j,i}D_i\ {}^{dust}K_i\ {}^{soil}h}{{}^{dust}K_i\ {}^{soil}h + \varepsilon} \tag{12}$$

Next, we non-dimensionalize parts of eqs. 7, 9, 10, and 12 using the following groups:

The ratio of dust to rock reactivity $S^*$ is written as:

$$S^* = \frac{{}^{dust}K_i}{{}^{rock}K_i} \tag{13a}$$

The dimensionless turnover timescale $t_i^*$ is expressed as:

$$t_i^* = \frac{{}^{rock}K_i\ {}^{soil}h}{\varepsilon}$$

(13b)

The dimensionless dust addition $D_i^*$ is defined as:

$$D_i^* = \frac{D_i}{\varepsilon N_{i,0}}$$

(13c)

We use these non-dimensional groups to calculate total solute flux from all rock and dust weathering ($^{total}F_j$):

$$^{total}F_j = \sum_i R_{j,i} N_{i,0} \varepsilon \left[1 - \frac{e^{-z^* t_i^*}}{t_i^* + 1} + \frac{D_i^* t_i^* S^*}{t_i^* S^* + 1}\right]$$

(14)

We then calculate the proportion of the total solute flux that comes from dust weathering as:

$$F_j^* = \frac{^{soil,dust}F_j}{^{total}F_j}$$

(15)

The full derivations of equations used for the weathering model and the explanations of variables are presented in Appendix A and B, respectively.

# 4. Application to rivers

We applied the steady-state rock and dust weathering model to estimate the magnitudes for $^{soil,dust}F_j$, $^{total,rock}F_j$, $^{total}F_j$, and $F_j^*$ that best explain the modern riverine solute fluxes of Si and SCM. Among the rivers used in section 2, we focused on the 14 rivers where all data necessary

for modeling are available (Table 3). We utilized a procedure that solves for model parameters (i.e., ${}^{rock}K_i$, $S^*$, $z^*$) by minimizing the misfit between observed and modeled Si and SCM fluxes.

## 4.1. Model input data and parameters

We used the measured quantities to estimate the rock and dust input to the weathering zone. For dust input, we used modern and LGM Si and SCM dust flux $D_i$ (mol $m^{-2}$ $yr^{-1}$) from Mahowald et al. (2006) described in section 2. To constrain $\varepsilon$, we subtracted the dust deposition rate from the sum of the physical and chemical weathering rates. Chemical and physical weathering rates were calculated as the product of runoff and total dissolved solids concentration (chemical) or total suspended solids concentration (physical) data from GEMS (G.E.M.S./Water, 2011). We assumed that these chemical and physical weathering rates exhibit congruence between weathering zone and riverine processes. However, we did not account for bedload in these weathering rate calculations, which may comprise a non-negligible or even major amount of the sediment fluxes in some basins.

We then calculated ${}^{soil,dust}F_j$, ${}^{total,rock}F_j$, and $F_j^*$ within the weathering zone using our weathering model, and we compare ${}^{total}F_j$ to riverine solute fluxes of Si and SCM. We assumed weathering of quartz solely contributes to the solute flux of Si, while weathering of non-quartz minerals contributes to solute flux of both Si and SCM. We used mineral concentrations ($N_i$) for quartz and non-quartz mineral phases (i.e., orthoclase, plagioclase, hornblende, and biotite) that are similar to average UCC (Rudnick and Gao, 2013 as partitioned by Hren et al., 2007 and White

and Brantley, 2003). We used concentrations of Si from quartz ($R_{Si,qz}N_{qz}$), Si from non-quartz mineral phases ($R_{Si,nqz}N_{nqz}$), and SCM from non-quartz mineral phases ($R_{SCM,nqz}N_{nqz}$), all of which are listed in Table 2. While we assumed congruence between modeled solute fluxes from the weathering zone and measured riverine solute fluxes, these relationships are likely complicated due to secondary mineral precipitation. To account for the loss of Si into secondary mineral precipitation, we applied a sequestration factor of 1.5 for predicted Si fluxes (Kim et al., 2017, 2014). We did not account a sequestration factor for Ca and Mg sinks because we used silicate-derived Ca + Mg fluxes that were separated from other sources (i.e., carbonate) and typically non-major fractions of total Ca + Mg fluxes (Moon et al., 2014). In our approach, we treat the reaction kinetics (i.e., ${}^{rock}K_i$ , $S^*$) as free parameters in the model, which are then optimized by comparison between model predictions and observed elemental fluxes.

To relate the modeled solute flux from the weathering zone (${}^{total}F_j$) to measured riverine discharges for the entire catchment, we considered the spatial locations and time periods where our weathering model is applicable. We assumed that periods and places that are frozen or dry are unfavorable for weathering. We identified areas and times of year where weathering may occur using global datasets of monthly temperature (1981-2010), precipitation (1958-2013), and potential evapotranspiration (1958-2013) (Abatzoglou et al., 2018; Willmott and Matsuura, 2001). In particular, we reprojected the climatic data to the same resolution (1 $km^2$ grid cells) and coordinate system (Lambert Azimuthal Equal Area projection) as Hydro1K. Then, we calculated the difference between precipitation and potential evapotranspiration (P – PET) for each month. Additionally, we identified, by pixel, months for which T > 0°C, and calculated

the fraction of an average year where soils are both not frozen and not dry (T > 0°C and P – PET > 0 mm $yr^{-1}$) for each grid cell. These fractions were used to weight the predicted weathering flux values (by pixel), which were then integrated across all points in each watershed to provide a prediction of modeled elemental discharges for each watershed, given $S^*$, $z^*$, and ${}^{rock}K_i$.

## 4.2. Model optimization

We optimized the weathering model to find the best-fit values for four parameters that minimize the misfit between modeled and measured solute fluxes for the modern condition. The four optimized parameters include ${}^{rock}K_i$ (converted from $yr^{-1}$ to $s^{-1}$) for quartz (${}^{rock}K_{qz}$), ${}^{rock}K_i$ for combined non-quartz phases (${}^{rock}K_{nqz}$), $S^*$, and $z^*$, where ${}^{rock}K_{qz}$ and ${}^{rock}K_{nqz}$ represent reaction rates for rock weathering from quartz and non-quartz mineral phases. Because we assume the same $k_i$ for dust and rock, $S^*$ represents the ratio of dust $S_i$ to rock $S_i$, which is proportional to their respective grain size differences (Ferrier and Kirchner, 2008). The model produces optimized $S^*$ but did not produce absolute grain sizes or $S_i$. The optimized ratio of saprolite to soil thicknesses ($z^*$) was used to infer the contribution from deep rock weathering relative to soil weathering For simplicity, we assumed a soil thickness of 1 m, similar to the mean upland soil thickness of 0.900 m (mean of individual basins: 0.524 – 1.08 m) calculated for all sampled basins using a global soil thickness dataset (Pelletier et al., 2015). Our approach of constant soil thickness is similar to a previous study of global erosion rates and dust fluxes (Arvin et al., 2017). Saprolite thickness can be inferred as a consequence of assumed soil

thickness and the optimized value of $z^*$. These four parameters were varied simultaneously with unbounded ranges.

We calculated the misfit as a residual sum of squares error between modeled and observed solute fluxes of Si and SCM. We did not assign any relative weighting for Si and SCM flux because the approximate range in observed Si and SCM discharges is similar. To directly search for global minima of misfit values, we conducted an optimization that uses the Nelder–Mead method, a downhill simplex algorithm (Nelder and Mead, 1965). With the obtained optimal parameter values, we calculated total predicted riverine fluxes from ${}^{soil,dust}F_j$, ${}^{soil,rock}F_j$, and ${}^{sap,rock}F_j$ by basin and for the sum of all sampled basins (hereinafter "all basins" or "all-basin"). We examined dust's contributions to silicate weathering fluxes ($F_j^*$) to determine the relative importance of dust and rock as sources of weathering products for individual basins and all basins.

## 4.3. Weathering model results

### 4.3.1. Model misfit and optimized parameter values

The optimal parameter values are reported in Table 2. The minimum misfit from the optimization is 0.0280 $mol^2\ m^{-4}\ yr^{-2}$, which is less than the data variation of 0.0298 $mol^2\ m^{-4}\ yr^{-2}$. The normalized error from our minimal misfit, calculated as the minimal misfit divided by data variance, is 0.940.

Our optimal parameter values are reasonable considering previous studies (Brantley et al., 2008; Clow and Drever, 1996; Hilley et al., 2010; Hren et al., 2007; Rudnick and Gao, 2013; Schulz and White, 1999; White and Brantley, 2003). Optimized ${}^{rock}K_{nqz}$ ($1.94 \times 10^{-13}$ $s^{-1}$) is similar to field-based measurements of non-quartz minerals such as hornblende ($1.3 \times 10^{-13} – 6.3 \times 10^{-15}$ $s^{-1}$) and biotite ($1.0 \times 10^{-11} – 6.3 \times 10^{-14}$ $s^{-1}$) and is slower than plagioclase ($1.9 \times 10^{-11}$ $s^{-1}$) by two orders of magnitude (Clow and Drever, 1996; Ferrier and Kirchner, 2008; Hilley et al., 2010). Optimized ${}^{rock}K_{qz}$ (0 $s^{-1}$) approaches zero and is therefore slower than field-based measurements ($3.2 \times 10^{-15}$ $s^{-1}$) and not an accurate representation of ${}^{rock}K_{qz}$ (Ferrier and Kirchner, 2008; Schulz and White, 1999). Additionally, quartz-derived weathering contributions are negligible due to the small value of optimized ${}^{rock}K_{qz}$ and would be similarly negligible if a field-based value of ${}^{rock}K_{qz}$ were used. Optimized $S^*$ ($1.08 \times 10^{2}$) is similar to a $S_i$ ratio of fine sand (~0.243 mm) to medium silt (~23.4 µm) (Udden, 1914). Optimized $z^*$ ($8.62 \times 10^{-15}$) demonstrates very low contributions from saprolite weathering and thus the vast majority of weathering coming from soil.

### 4.3.2. Sensitivity for model parameters

Although optimization identifies parameter values with the minimum misfit between predicted and observed fluxes, it does not allow us to examine how sensitive our model results are based on the varying ranges of model parameters. To better show the distribution of misfit values, we calculate the normalized misfit errors with varying ranges of ${}^{rock}K_{nqz}$ and $S^*$ (Figure A1). Due

to the small contribution from weathering from quartz (${}^{rock}K_{qz}$) and small contribution from saprolite ($z^*$), we did not consider the variations from those two parameters. The error space calculated for ${}^{rock}K_{nqz}$ and $S^*$ shows that the normalized error similar to the minimum value (0.940 – 0.96) falls over both a narrow range of ${}^{rock}K_{nqz}$ (~$10^{-12.6}$ – $10^{-12.8}$ $s^{-1}$) and a wider range of $S^*$ values of ~$10^1$ to greater than $10^4$. This indicates that in proximity to optimized ${}^{rock}K_{nqz}$, our misfit error calculation is more sensitive to perturbations within ${}^{rock}K_{nqz}$ than $S^*$. This relative difference is more pronounced at higher error values (0.96 – 1.00).

### 4.3.3. Predicted weathering fluxes and dust contribution

Using the optimal parameter values from 4.3.1, we calculate total predicted solute fluxes from rock and dust weathering and the predicted dust contributions to total silicate weathering fluxes for the modern condition (Table 3). We explore predicted riverine fluxes of both individual rivers and global fluxes. For individual rivers, the range of predicted total Si flux (mol $m^{-2}$ $yr^{-1}$) is $6.92 \times 10^{-3}$ – $7.53 \times 10^{-2}$, while that of SCM is $1.96 \times 10^{-3}$ – $2.13 \times 10^{-2}$. The range of measured total flux for Si (mol $m^{-2}$ $yr^{-1}$) is $4.24 \times 10^{-4}$ – $8.92 \times 10^{-2}$, while that of SCM is $1.36 \times 10^{-3}$ – $1.51 \times 10^{-1}$. The predicted Si and SCM fluxes of our steady-state weathering model show good correlation with the observed Si and SCM fluxes ($R^2$ = 0.474 for Si and 0.472 for SCM excluding two outliers) (Figure 3). For all-basin flux from 14 rivers, predicted Si flux is 23% overpredicted, while predicted SCM flux is 35% underpredicted relative to observed riverine flux from all basins.

Our model results show that an appreciable fraction of silicate weathering fluxes could be dust-derived. The ratio of dust-derived flux to total flux is equivalent to $F_j^*$, or the fraction of flux that is dust-derived. $F_{Si}^*$ and $F_{SCM}^*$ varies from 7.83% (Mackenzie) to 63.5% (Mississippi) (Table 3). The overall magnitude of $F_j^*$ based on fluxes from all basins is 41% for both Si and SCM. The dust contribution to total Ca + Mg flux is 8.1%. For the 35 rivers used in this study where this information is available, carbonate weathering contributes 22 – 97% of Ca + Mg flux (63% for all rivers combined and 78% for all 14 model-sampled rivers combined), while silicate weathering contributes 2 – 60% of Ca + Mg flux (16% for all rivers combined and 19% for all 14 model-sampled rivers combined). Thus, dust and rock weathering are predicted to be within the same order of magnitude.

In addition, by applying the modeled dust deposition during LGM, we calculate total predicted solute fluxes, the predicted dust contributions to total silicate weathering fluxes, and the degrees of enhancement from the steady-state dust and rock weathering fluxes during LGM. Overall modeled fluxes for Si and SCM during LGM are both greater than and within the same order of magnitude of their modern counterparts. The range in the proportion of predicted (both Si and SCM) flux that is dust-derived for the LGM is 18.3% – 96.9%. For individual rivers, the range of LGM RDL discharge enhancement due to dust is 5.57% – 2589% for both Si and SCM independently. Due to negligible contributions from chemical weathering of quartz, enhancements are entirely from dust weathering of non-quartz minerals and thus have the same magnitudes for Si and SCM discharges. Two sampled rivers, the Mississippi and the Kolyma, exceed 1000% LGM enhancement for both Si and SCM.

# 5. Discussion

## 5.1. Assumptions and limitations

Our analysis quantifying the dust and rock weathering contribution to global silicate weathering fluxes demonstrates that dust weathering could be a substantial component of total silicate weathering fluxes in some places. However, our approach is based on limited data and simplified model assumptions, which can introduce uncertainties into our estimates. First, our analyses are based on a small number of rivers. We used 22 (Si) and 35 (SCM) rivers for our mass balance calculation and 14 rivers to optimize our weathering model. These rivers were selected based on data availability for adequate contemporaneous ion concentrations, total dissolved and suspended loads, and water runoff measurements (e.g., Moon et al., 2014). Although the number of rivers that we used in our weathering model is small, these rivers account for approximately 24% of total global runoff excluding interior runoff (G.E.M.S./Water, 2011). It is encouraging that our dust and rock weathering model is somewhat successful in predicting reasonable global silicate weathering fluxes, but larger spatiotemporal coverage of riverine fluxes would lead to a higher degree of constraint and would produce more robust flux estimates.

Second, we assume simple chemical composition of geological materials such that average bedrock and dust compositions are similar to that of average UCC. However, chemical

composition of bedrock and dust can vary substantially by location (Hartmann and Moosdorf, 2012; Lawrence and Neff, 2009), which can impact riverine chemical fluxes (e.g., Moon et al., 2014). Regarding dust composition, average chemical composition may vary from our assumed values depending on the dust sources (e.g., local vs global). The limited spatial coverage of dust mineralogy measurements is not sufficient for constructing reliable estimates for our samples. However, global averages based on compiled and original measurements by Lawrence and Neff (2009) show major elements such as Si, Mg, and Ca, are within 20% of UCC averages, and silicate minerals such as quartz, feldspar, and phyllosilicates are most abundant in aeolian dust. These findings generally align with our assumption of similar dust and UCC composition. However, they also find substantial local variations in chemistry, especially Ca and trace metals, likely due to the differences in local dust source materials, transport distance, and grain size distribution (Mahowald et al., 2014, Lawrence and Neff, 2009). There is evidence that carbonate weathering could contribute a substantial proportion of total Ca and/or Mg solute fluxes even at low (~1% of soil parent material by mass) carbonate proportions of the total lithology (Waldbauer and Chamberlain, 2005; Jacobson et al., 2002; Moon et al., 2014). This disproportionate effect of carbonate weathering could also apply to dust deposition and subsequent weathering fluxes from dust. In this work, we attempted to subdivide the silicate contribution to solute fluxes into rock and dust contributions. For chemical flux estimates from rivers, we used silicate-derived Ca + Mg fluxes that have excluded carbonate contributions using the inverse model of the chemical sources (Moon et al., 2014) to exclude inputs from carbonate weathering from rock or dust. To better constrain the chemical composition of dust deposition, we would need precise information on dust source and climatic conditions that

determine transport paths, grain sizes, and precipitation rates. Currently, such information is not available globally. Furthermore, it is unknown how those conditions have varied over the timescales of weathering in the shallow subsurface (~1 – 1000 ka) from this study.

Third, we used simplified weathering laws and environmental conditions and assumed congruence between elemental fluxes leaving the weathering zone and riverine solute fluxes. Our modeled environment for the shallow subsurface allows two layers, soil and saprolite, and assumes a constant soil thickness of 1 m. The 1 m thickness of soil is within the range of estimated soil thickness for our 14 basins (0.524 – 1.08 m) based on a global map of soil thickness (Pelletier et al., 2015). We do not have a general model of how dust assimilates into soil at different sites or how dust input affects soil thickness or turnover time. We also assume simple linear reaction kinetics that do not consider hydrologic residence time and time-varying changes of mineral $S_i$ or weathering reactions (White and Brantley, 2003). We also do not treat depositional environments like floodplains differently from erosional environments. Depositional environments may comprise an appreciable proportion of Earth's land area, including within some of our sampled basins (e.g., Bickle et al., 2018). Although weathering processes in these erosional vs. depositional environments may behave differently, we apply our model to entire catchment areas under the assumption that dust weathering may still comprise an appreciable fraction of weathering from depositional areas.

Fourth, although it is interesting to find the potential enhancement of weathering during the LGM, these analyses are based on limited information and thus speculation surrounding these

results should be minimized. The only condition that is varied to estimate weathering fluxes between our modern and LGM cases is modeled dust precipitation. Climatic and hydrologic conditions during the LGM certainly differ from modern conditions, especially at high latitudes, thus using model parameters (e.g., ${}^{rock}K_i$, $S^*$) and environmental conditions (e.g., PET, temperature) based on modern conditions may not accurately predict solute fluxes during the LGM. However, due to the lack of LGM riverine flux data as well as LGM high-resolution modeled climatic and hydrologic conditions, we cannot directly apply our weathering model to LGM conditions. Thus, our weathering enhancements during LGM should be considered as theoretical estimates based solely on variations in modeled dust deposition.

Due to these limitations of existing datasets, we did not seek to construct a complicated model with many unknown parameters. We intentionally built a simple model that could utilize existing data to constrain certain model parameter values but allows some estimate of the uncertainties within some of the key parameters. Our goal is to calculate a first-order approximation of dust and rock silicate weathering fluxes and to assess the potential importance of dust's contribution. We take advantage of the best currently available global data in our model, but we acknowledge that the sample size and spatial coverage of our riverine data are limited. The relative differences between predicted and observed all-basin fluxes are +23% (Si) and -35% (SCM). These differences are potentially explained by variations in rock and dust composition, modeled dust flux, Si sequestration factor, the limited number of river samples, and simplified model assumptions. Our modeling work describes the first attempt for global analysis of dust and rock silicate weathering given limited data availability.

Current data limitations imply a necessity for both more substantial data acquisition and further theoretical investigation to more accurately constrain the relative impacts of dust and rock on weathering fluxes on regional and global scales.

## 5.2. Importance of dust weathering in the global weathering budget

Our model results demonstrate that an appreciable fraction (~41% based on 14 rivers) of silicate weathering fluxes could be derived from dust. Our analyses suggest that dust weathering should be considered in quantifications of total weathering, as it could comprise a substantial fraction of silicate weathering in most rivers. Our work did not, and did not attempt to, refute or disprove the current ubiquitous model that assumes that rock weathering dominates global weathering fluxes. Rather, this study attempts to explore the potential role that dust weathering may play in the global weathering budget, especially regarding silicate weathering. Importantly, our results suggest that dust inputs to silicate weathering could account for almost as much as silicate rock weathering, and as such, could be important in affecting changes to global biogeochemical cycles, now and in Earth's past.

Interestingly, although the mass inputs into the weathering zone from bedrock are usually much greater than that of dust, the likely higher reactivity of dust may allow it to weather more completely than rock. In contrast, substantial mechanical disaggregation of rock by physical, biological, and chemical processes may be necessary to substantially increase the mineral $S_i$.

Based on our optimized value for *S** and assuming that the chemical weathering rate is proportional to specific surface area (Ferrier and Kirchner, 2008), we expect dust to be > 200 times more reactive than rock in our studied rivers. The sensitivity analysis based on the ranges of ${}^{rock}K_{nqz}$ and *S** show that a range of *S**, in which dust is roughly 100-1000 more reactive than rock, produce misfit values similar to that from our optimal parameter values. This overall *S** range supports the idea that dust may quickly weather to completion in cases where rock does not.

## 5.3. Implications for global weathering feedbacks

Climate and dust deposition conditions during the LGM were both different from today, which implies that the distribution of weathering might also be different. For example, dust deposition rates were generally much greater during the LGM (Mahowald et al., 2006) because of the action of glaciers and ice sheets in producing fine material. Our modeling analysis shows that for most basins, the increased dust deposition leads to positive enhancement in weathering fluxes during the LGM. If this were the case, it sets up the potential for a positive feedback, in which the weathering of rock and dust leads to drawdown of sufficient $CO_2$ to further cool the climate, expanding the ice sheets and potentially further enhancing dust fluxes. However, our estimates of dust weathering during the LGM may be an overestimate. For example, two sampled high-latitude rivers in our model predictions, the Mississippi and the Kolyma, show LGM enhancement of riverine Si and SCM of 1000% or more. In fact, extensive loess deposits cover a large proportion of the Mississippi basin today (Aleinikoff et al., 1999;

Roberts et al., 2003), which represents a net accumulation of dust without complete (but not necessarily substantial) weathering. Also, it is possible that a lower proportion of the global land surface was available for chemical weathering due to burial under ice during the LGM, preventing these glaciated areas from contributing substantially to weathering discharges. The interplay between enhanced dust flux, accumulation of unweathered dust on landscapes, and glacial cover is a central question as to how weathering discharges may change over glacial-interglacial cycles. Incorporating these factors will be an important step in understanding how climate and Earth-surface process changes may alter global biogeochemical cycling in Earth's past.

# 6. Conclusion

This study finds that 7.8 – 63% of the silicate-derived dissolved ions in rivers could be derived from dust weathering. This finding does not rule out the long-held view that rock weathering dominates chemical fluxes in rivers, but highlights the possibility that dust weathering could account for a substantial fraction of the global silicate weathering budget. We find that model-predicted rock and dust silicate weathering are typically within the same order of magnitude for Si and SCM discharges. The rapid reaction of dust and its appreciable contribution to silicate weathering implies that characterizing dust properties (e.g., size distribution, composition) for the source, transport, and deposition of global dust flux is important for quantifying global silicate weathering budgets. In addition, dust could be an important driver of global chemical weathering, biogeochemical cycling, and climate-weathering feedbacks on geologic timescales.

# Appendix A. Detailed Description of Weathering Model

In our steady-state weathering model, we account for the weathering of two material phases (rock and dust) and two weathering zones (saprolite and soil) in the subsurface. We quantify the total solute flux of (1) rock weathering within the saprolite zone (where it is unmixed), (2) rock weathering in the mobile soil (where it is mixed), and (3) dust weathering in the mobile soil.

In the case of saprolite, we assume that fresh bedrock moves through saprolite at a velocity equal to the erosion rate. In this case, the composition of weathered bedrock within saprolite changes with the distance from the bedrock-saprolite boundary due to chemical weathering. Assuming a steady state (i.e., $\frac{dN_i}{dt} = 0$), eq. (1) for saprolite becomes:

$$\varepsilon \frac{d^{sap,rock}N_i}{dz} = -^{rock}K_i \, ^{sap,rock}N_i \tag{A1}$$

By integrating eq. (A1), we calculate the concentration of a specific mineral $i$ ($N_i(z)$, mol m$^{-3}$) within the saprolite above the distance from the bedrock-saprolite boundary ($z$, m) as:

$$^{sap,rock}N_i(z) = N_{i,0}e^{-\frac{^{rock}K_i \, z}{\varepsilon}} \tag{A2}$$

where $N_{i,0}$ is the concentration of the particular mineral phase $i$ in the unweathered, fresh bedrock at the bottom of the saprolite. In this case, the volume rate of solute production ($B_{j,i}$, mol m$^{-3}$ yr$^{-1}$) for a particular ion $j$ is:

$$^{sap,rock}B_{j,i}(z) = R_{j,i}{}^{rock}K_i \; ^{sap,rock}N_i(z) \; = R_{j,i}{}^{rock}K_i N_{i,0} e^{-\frac{^{rock}K_i \, z}{\varepsilon}} \tag{A3}$$

We then integrate $^{sap,rock}B_{j,i}$ across the saprolite thickness for a mineral phase $i$ to produce the solute flux for a specific solute phase $j$ due to saprolite weathering from a mineral phase $i$ ($^{sap,rock}F_{j,i}$, mol m$^{-2}$ yr$^{-1}$) and apply the condition that $^{sap,rock}F_{j,i}(0) = 0$ to obtain:

$$^{sap,rock}F_{j,i} = \int_0^{z_s} {}^{sap,rock}B_{j,i}(z)\, dz = -R_{j,i}N_{i,0}\varepsilon e^{-\frac{^{rock}K_i \, z_s}{\varepsilon}} + R_{j,i}N_{i,0}\varepsilon \tag{A4}$$

where $z_s$ is the distance from the bedrock-saprolite boundary to soil-saprolite boundary, which equals $^{sap}h$ . This allows us to simplify the equation for $^{sap,rock}F_{j,i}$ as:

$$^{sap,rock}F_{j,i} = R_{j,i}N_{i,0}\varepsilon\left[1 - e^{-\frac{^{rock}K_i \; ^{sap}h}{\varepsilon}}\right] \tag{A5}$$

Then, we sum the solute rates for a specific solute phase $j$ from all mineral phases to produce the total solute flux from rock weathering within saprolite ($^{sap,rock}F_j$, mol m$^{-2}$ yr$^{-1}$) as:

$$^{sap,rock}F_j = \sum_i {}^{sap,rock}F_{j,i} \; = \sum_i R_{j,i}N_{i,0}\varepsilon\left[1 - e^{-\frac{^{rock}K_i \; ^{sap}h}{\varepsilon}}\right] \tag{A6}$$

Next, we consider rock weathering in the mixed soil. We assume a steady state (i.e., $\frac{dN_i}{dt} = 0$) and mixed soil (i.e., $\frac{dN_i}{dz} = 0$), the addition and removal of rock material in soil is expressed in source and sink term ($S_i$) in eq. (1). We account that flux of $N_i$ entering to the base of the soil from the top of the saprolite and exiting from the top of the soil is distributed within the soil by dividing by the soil thickness ($^{soil}h$, m) to yield a volumetric rate of phase addition and physical removal in eq. (8), respectively. We also account for chemical reaction. Thus, eq. (1) for rock weathering within the soil is modified as:

$$\frac{\varepsilon N_{i,0} e^{-\frac{^{rock}K_i \, ^{sap}h}{\varepsilon}}}{^{soil}h} - \frac{\varepsilon^{soil,rock} N_i}{^{soil}h} - \, ^{rock}K_i \, ^{soil,rock}N_i = 0 \tag{A7}$$

With this, eq. (A6) produces the following solution for $^{soil,rock}N_i$ as:

$$^{soil,rock}N_i = \frac{\varepsilon N_{i,0} e^{-\frac{^{rock}K_i \, ^{sap}h}{\varepsilon}}}{^{rock}K_i \, ^{soil}h + \, \varepsilon} \tag{A8}$$

In this case, the volume rate of solute production ($B_{j,i}$, mol m$^{-3}$ yr$^{-1}$) for a particular ion from rock weathering within the soil is:

$$^{soil,rock}B_{j,i} = R_{j,i} \, ^{rock}K_i \, ^{soil,rock}N_i = \frac{R_{j,i} \, ^{rock}K_i \varepsilon N_{i,0} e^{-\frac{^{rock}K_i \, ^{sap}h}{\varepsilon}}}{^{rock}K_i \, ^{soil}h + \, \varepsilon} \tag{A9}$$

As before, we obtain the solute flux due to rock weathering in the soil for a mineral phase $i$ ($^{soil,rock}F_{j,i}$, mol m$^{-2}$ yr$^{-1}$) in terms of weathering products integrated over the soil thickness. With the equivalence of $^{soil}h = z_0 - z_s$ where $z_0$ and $z_s$ are the distances from the bedrock-

saprolite interface to the top of the soil and the top of saprolite, respectively, we can rewrite the equation for ${}^{soil,rock}F_{j,i}$ as:

$$ {}^{soil,rock}F_{j,i} = \int_{z_s}^{z_0} {}^{soil,rock}B_{j,i}\, dz = \frac{R_{j,i} N_{i,0} \varepsilon\, {}^{rock}K_i\, {}^{soil}h\; e^{-\frac{{}^{rock}K_i {}^{sap}h}{\varepsilon}}}{{}^{rock}K_i {}^{soil}h + \varepsilon} \quad \text{(A10)} $$

We sum the solute rates for a specific solute phase $j$ from all mineral phases to produce the total solute flux from rock weathering within soil (${}^{soil,rock}F_j$, mol m$^{-2}$ yr$^{-1}$) as:

$$ {}^{soil,rock}F_j = \sum_i \frac{R_{j,i} N_{i,0} \varepsilon\, {}^{rock}K_i\, {}^{soil}h\; e^{-\frac{{}^{rock}K_i {}^{sap}h}{\varepsilon}}}{{}^{rock}K_i {}^{soil}h + \varepsilon} \quad \text{(A11)} $$

Together, this produces a total rock weathering flux from soil and saprolite as:

$$ {}^{total,rock}F_j = {}^{sap,rock}F_j + {}^{soil,rock}F_j = \sum_i R_{j,i} N_{i,0} \varepsilon \left[ 1 - \frac{\varepsilon\, e^{-\frac{{}^{rock}K_i\, {}^{soil}h\, z^*}{\varepsilon}}}{{}^{rock}K_i\, {}^{soil}h + \varepsilon} \right] \quad \text{(A12)} $$

where $z^* = \frac{{}^{sap}h}{{}^{soil}h}$.

Finally, utilizing a dust-specific reaction rate ${}^{dust}K_i$(yr$^{-1}$) due to dust's high reactive surface area and dust input flux $D_i$ (mol m$^{-2}$ yr$^{-1}$) of the mineral phase $i$, we derive the solute flux due to dust weathering (${}^{soil,dust}F_j$) within the soil. In the case of dust weathering, eq. (1) becomes:

$$\frac{D_i}{{}_{soil}h} - \frac{\varepsilon^{soil,dust}N_i}{{}_{soil}h} - {}^{dust}K_i \, {}^{soil,dust}N_i = 0$$

(A13)

Then, eq. (A14) has the following solution:

$${}^{soil,dust}N_i = \frac{D_i}{{}_{dust}K_i \, {}_{soil}h + \varepsilon}$$

(A14)

Similarly to rock weathering in the soil, $B_{j,i}$ becomes:

$${}^{soil,dust}B_{j,i} = R_{j,i} \, {}^{dust}K_i \, {}^{soil,dust}N_i = R_{j,i} \frac{D_i \, {}^{dust}K_i}{{}_{dust}K_i \, {}^{soil}h + \varepsilon}$$

(A15)

This allows us to define the solute flux produced by dust weathering in the soil as the following:

$${}^{soil,dust}F_{j,i} = \int_{z_s}^{z_0} {}^{soil,dust}B_{j,i} \, dz = R_{j,i} \frac{D_i \, {}^{dust}K_i \, {}^{soil}h}{{}_{dust}K_i \, {}^{soil}h + \varepsilon}$$

(A16)

Then, we sum the solute rates for a specific solute phase $j$ from all mineral phases to produce the total solute flux from dust weathering within soil ( ${}^{soil,dust}F_j$, mol m$^{-2}$ yr$^{-1}$) as:

$${}^{soil,dust}F_j = \sum_i R_{j,i} \frac{D_i \, {}^{dust}K_i \, {}^{soil}h}{{}_{dust}K_i \, {}^{soil}h + \varepsilon}$$

(A17)

To simplify, we define the following non-dimensional groups:

The ratio of dust to rock reactivity $S^*$:

$$S^* = \frac{{}^{dust}K_i}{{}^{rock}K_i}$$

(A18a)

The dimensionless turnover timescale $t_i^*$:

$$t_i^* = \frac{^{rock}K_i \, ^{soil}h}{\varepsilon}$$

(A18b)

The dimensionless dust addition $D_i^*$:

$$D_i^* = \frac{D_i}{\varepsilon N_{i,0}}$$

(A18c)

Using these non-dimensional groups, we can now rewrite eqs. A12 and A17:

$$^{total,rock}F_j = \sum_i R_{j,i} N_{i,0} \varepsilon \left[1 - \frac{e^{-z^* t_i^*}}{t_i^* + 1}\right]$$

(A19)

$$^{soil,dust}F_j = \sum_i R_{j,i} D_i^* N_{i,0} \varepsilon \frac{t_i^* S^*}{t_i^* S^* + 1}$$

(A20)

We now define the solute flux produced from all rock and dust sources $^{total}F_j$:

$$^{total}F_j = \sum_i R_{j,i} N_{i,0} \varepsilon \left[1 - \frac{e^{-z^* t_i^*}}{t_i^* + 1} + \frac{D_i^* t_i^* S^*}{t_i^* S^* + 1}\right]$$

(A21)

Using eqs. A20 and A21, the proportion of the total solute flux that comes from dust weathering $F_j^*$ becomes:

$$F_j^* = \frac{^{soil,dust}F_j}{^{total}F_j}$$

(A22)

# Appendix B. Explanation of Variables

| Variable | Description |
|---|---|
| $i$ | Mineral phases (quartz (qz), non-quartz silicate minerals (nqz)) |
| $j$ | Solutes (Si, silicate-derived Ca + Mg (SCM)) |
| $a$ | Weathering zones (saprolite, soil) |
| $b$ | Materials (rock, dust) |
| $t$ | Time (yr) |
| ${}^{a}h$ | Layer thickness (m) for a specific weathering zone $a$ |
| $z$ | Distance upward from the bedrock-saprolite boundary |
| $\varepsilon$ | Erosion rate (m $yr^{-1}$) |
| $R_{j,i}$ | Stoichiometric ratio between the reacting mineral phase $i$ and the produced solute $j$ |
| ${}^{a,b}N_i$ | Concentration of a particular mineral phase $i$ (mol $m^{-3}$) for material $b$ within weathering zone $a$ |
| ${}^{b}K_i$ | Reaction rate of a particular mineral phase $i$ for material $b$ ($yr^{-1}$ or $s^{-1}$) |
| $k_i$ | Kinetics constant of reaction a particular mineral phase $i$ ($m^{-2}$ $yr^{-1}$) |
| ${}^{b}S_i$ | Reactive surface area of a particular mineral phase $i$ for material $b$ ($m^2$) |
| ${}^{a,b}P_i$ | Volumetric rate of mineral $i$ phase addition or removal to weathering zone $a$ for material $b$ (mol $m^{-3}$ $yr^{-1}$) |
| ${}^{a,b}B_{j,i}$ | Volumetric rate of solute $j$ production from mineral $i$ for material $b$ in weathering zone $a$ (mol $m^{-3}$ $yr^{-1}$) |
| ${}^{a,b}F_{j,i}$ | Solute flux $j$ produced from mineral $i$ for material $b$ within weathering zone $a$ (mol $m^{-2}$ $yr^{-1}$) |
| $D_i$ | Dust input flux (mol $m^{-2}$ $yr^{-1}$) from mineral $i$ |
| $z^*$ | Ratio of saprolite to soil thickness |

| | |
|---|---|
| $S^*$ | Ratio of dust to rock reaction rate $S^* = \frac{dust_{K_i}}{rock_{K_i}}$ |
| ${t_i}^*$ | Non-dimensional time equivalent to $t_i^* = \frac{rock_{K_i} soil_h}{\varepsilon}$ |
| ${D_i}^*$ | Non-dimensional dust flux equivalent to $\frac{D_i}{\varepsilon N_{i,0}}$ |
| ${F_j}^*$ | The proportion of total solute fluxes constituted by dust-derived solute flux |

# Tables

Table 1. Dust deposition, riverine dissolved load, and their proportions in 44 rivers

| River | Basin Area | Station Latitude | Station Longitude | Modern Dust Deposition | LGM Dust Deposition | Cation Fraction (Ca + Mg) (Moon et al., 2014) | | Riverine dissolved load | | | | Dust deposition* | | | | $\delta_j$* | |
|---|---|---|---|---|---|---|---|---|---|---|---|---|---|---|---|---|---|
| | | | | | | | | Discharge | | Flux | | Discharge | | Flux | | | |
| | | | | | | | | Si | SCM | Si | SCM | Si | SCM | Si | SCM | $\delta_{Si}$* | $\delta_{SCM}$* |
| | ($10^9$ m$^2$) | (°) | (°) | ($10^9$ kg yr$^{-1}$) | ($10^9$ kg yr$^{-1}$) | From Carbonate | From Silicate | ($10^9$ mol yr$^{-1}$) | ($10^9$ mol yr$^{-1}$) | ($10^{-3}$ mol m$^{-2}$ yr$^{-1}$) | ($10^{-3}$ mol m$^{-2}$ yr$^{-1}$) | ($10^9$ mol yr$^{-1}$) | ($10^9$ mol yr$^{-1}$) | ($10^{-3}$ mol m$^{-2}$ yr$^{-1}$) | ($10^{-3}$ mol m$^{-2}$ yr$^{-1}$) | | |
| Amazon | 4689 | -1.94694 | -55.51083 | 22.8 | 33.9 | 0.800 | 0.160 | 418 | 190 | 89.2 | 40.6 | 253 | 28.6 | 53.9 | 6.11 | 0.605 | 0.150 |
| Cauvery | 67.6 | 10.94278 | 78.44139 | 0.433 | 1.30 | 0.650 | 0.230 | | 4.39 | | 64.9 | 4.80 | 0.543 | 70.9 | 8.03 | | 0.124 |
| Chang Jiang | 1458 | 30.58306 | 114.82889 | 13.0 | 33.2 | 0.910 | 0.060 | | 41.2 | | 28.3 | 144 | 16.3 | 99.0 | 11.2 | | 0.397 |
| Colorado | 432 | 36.01528 | -114.73778 | 54.5 | 1.74 | 0.320 | 0.600 | 2.06 | 24.7 | 4.77 | 57.1 | 604 | 68.5 | 1400 | 159 | 1.00 | 1.00 |
| Columbia | 625 | 45.61250 | -122.02639 | 1.42 | 2.85 | 0.840 | 0.140 | 24.3 | 14.0 | 38.9 | 22.4 | 15.7 | 1.78 | 25.1 | 2.84 | 0.645 | 0.127 |
| Congo | 3623 | -4.28227 | 15.30080 | 29.2 | 46.2 | 0.610 | 0.370 | 99.1 | 48.2 | 27.4 | 13.3 | 324 | 36.7 | 89.4 | 10.12 | 1.00 | 0.761 |
| Dalalven | 28.9 | 60.58333 | 17.45000 | 0.0543 | 0.373 | 0.800 | 0.170 | 0.905 | 0.327 | 31.4 | 11.3 | 0.602 | 0.0682 | 20.9 | 2.36 | 0.666 | 0.209 |
| Danube | 179 | 47.61000 | 19.09667 | 1.81 | 22.5 | 0.900 | 0.040 | | 3.76 | | 21.0 | 20.0 | 2.27 | 112 | 12.6 | | 0.603 |
| Ebro | 12.1 | 42.41667 | -2.20500 | 0.0781 | 0.0926 | 0.610 | 0.210 | 0.188 | 1.83 | 15.5 | 151 | 0.865 | 0.0980 | 71.3 | 8.08 | 1.00 | 0.0536 |
| Garonne | 51.0 | 44.51667 | 0.06667 | 0.405 | 0.508 | 0.930 | 0.020 | | 0.371 | | 7.28 | 4.49 | 0.508 | 88.0 | 10.0 | | 1.00 |
| Glama | 40.6 | 59.58833 | 11.09667 | 0.0647 | 0.349 | 0.840 | 0.130 | | 0.390 | | 9.61 | 0.718 | 0.0813 | 17.7 | 2.00 | | 0.209 |
| Godavari | 307 | 17.25000 | 81.66667 | 1.31 | 2.35 | 0.590 | 0.310 | | 26.6 | | 86.4 | 14.5 | 1.64 | 47.1 | 5.33 | | 0.0617 |
| Guadiana | 49.9 | 38.88250 | -6.97750 | 0.443 | 0.424 | 0.660 | 0.280 | | 0.54 | | 10.8 | 4.91 | 0.557 | 98.6 | 11.2 | | 1.00 |
| Huang He | 977 | 36.73333 | 116.98333 | 24.3 | 96.5 | 0.510 | 0.330 | | 13.9 | | 14.2 | 269 | 30.5 | 275 | 31.2 | | 1.00 |
| Hudson | 22.7 | 42.75222 | -73.68944 | 0.121 | 0.580 | | | 0.896 | | 39.5 | | 1.34 | 0.152 | 59.0 | 6.69 | 1.00 | |
| Indus | 1130 | 25.23000 | 68.31167 | 37.1 | 56.6 | | | | | | | 411 | 46.5 | 363 | 41.2 | | |
| Kolyma | 536 | 68.71889 | 158.79889 | 0.593 | 77.7 | 0.740 | 0.170 | 6.98 | 5.00 | 13.0 | 9.34 | 6.57 | 0.744 | 12.3 | 1.39 | 0.941 | 0.149 |
| Krishna | 268 | 16.51667 | 80.61667 | 1.99 | 4.12 | 0.690 | 0.140 | | 4.98 | | 18.6 | 22.1 | 2.50 | 82.2 | 9.31 | | 0.502 |
| Lena | 2372 | 70.66667 | 127.33333 | 6.75 | 2583 | | | 21.6 | | 9.11 | | 74.8 | 8.47 | 31.5 | 3.57 | 1.00 | |
| Limpopo | 201 | -22.22500 | 29.99050 | 0.398 | 0.533 | 0.710 | 0.200 | 0.0854 | 0.273 | 0.424 | 1.36 | 4.41 | 0.500 | 21.9 | 2.48 | 1.00 | 1.00 |
| Mackenzie | 1643 | 67.45833 | -133.70000 | 0.598 | 4.56 | 0.890 | 0.080 | 15.4 | 22.3 | 9.36 | 13.6 | 6.63 | 0.751 | 4.04 | 0.457 | 0.431 | 0.0336 |
| Magdalena | 7.81 | 3.45056 | -76.47611 | 0.0293 | 0.0371 | 0.710 | 0.190 | | 0.422 | | 54.0 | 0.324 | 0.0367 | 41.6 | 4.71 | | 0.0871 |
| Mekong | 763 | 10.70000 | 105.15694 | 1.10 | 1.55 | 0.800 | 0.160 | 5.70 | 4.57 | 7.47 | 5.98 | 12.2 | 1.38 | 16.0 | 1.81 | 1.00 | 0.303 |
| Mississippi | 2928 | 32.31250 | -90.90694 | 34.5 | 675 | 0.880 | 0.070 | 81.5 | 51.9 | 27.8 | 17.7 | 383 | 43.3 | 131 | 14.8 | 1.00 | 0.834 |
| N. Dvina | 315 | 64.14306 | 41.92222 | 1.29 | 7.59 | 0.690 | 0.290 | 5.12 | 18.6 | 16.3 | 58.9 | 14.3 | 1.62 | 45.3 | 5.13 | 1.00 | 0.0871 |
| Narmada | 90.2 | 21.91667 | 73.65000 | 0.490 | 0.895 | 0.780 | 0.130 | | 2.34 | | 26.0 | 5.44 | 0.616 | 60.3 | 6.83 | | 0.263 |
| Neva | 232 | 59.83333 | 30.50000 | 1.01 | 5.82 | 0.780 | 0.120 | 0.254 | 3.88 | 1.09 | 16.7 | 11.2 | 1.27 | 48.4 | 5.49 | 1.00 | 0.328 |
| Niger | 119 | 12.86667 | -7.55111 | 5.25 | 7.21 | | | | | | | 58.2 | 6.59 | 491 | 55.6 | | |
| Nile | 1688 | 15.50000 | 32.46333 | 89.7 | 106 | 0.770 | 0.140 | | 3.82 | | 2.26 | 994 | 113 | 589 | 66.7 | | 1.00 |
| Oder | 112 | 53.03500 | 14.31278 | 0.611 | 17.7 | 0.690 | 0.130 | | 4.16 | | 37.2 | 6.78 | 0.767 | 60.6 | 6.87 | | 0.185 |
| Orinoco | 818 | 8.14319 | -63.60739 | 3.72 | 5.28 | 0.800 | 0.180 | 54.0 | 17.0 | 66.1 | 20.8 | 41.2 | 4.67 | 50.4 | 5.71 | 0.762 | 0.274 |
| Parana | 2636 | -32.82690 | -60.69480 | 63.6 | 65.8 | 0.330 | 0.280 | | 42.3 | | 16.0 | 705 | 79.9 | 268 | 30.3 | | 1.00 |
| Po | 1.69 | 46.16472 | 8.91139 | 0.0197 | 0.0516 | 0.970 | 0.020 | 0.140 | 0.0365 | 83.4 | 21.6 | 0.218 | 0.0247 | 130 | 14.7 | 1.00 | 0.678 |
| Rhone | 10.2 | 46.16278 | 5.97778 | 0.107 | 0.198 | 0.960 | 0.020 | 0.344 | 0.227 | 33.8 | 22.3 | 1.18 | 0.134 | 116 | 13.2 | 1.00 | 0.590 |
| Rio Grande | 492 | 25.87639 | -97.45417 | 17.7 | 5.84 | 0.220 | 0.530 | 0.0473 | 0.387 | 0.0963 | 0.787 | 197 | 22.3 | 400 | 45.3 | 1.00 | 1.00 |
| Seine | 31.9 | 48.85000 | 2.35000 | 0.189 | 0.386 | | | | | | | 2.09 | 0.237 | 65.7 | 7.44 | | |
| St. Lawrence | 784 | 45.00611 | -74.79528 | 4.73 | 39.5 | | | 1.57 | | 2.00 | | 52.4 | 5.93 | 66.8 | 7.57 | 1.00 | |
| Tagus | 68.3 | 39.22639 | -8.67611 | 0.483 | 0.511 | | | | | | | 5.35 | 0.607 | 78.4 | 8.88 | | |
| Tapti | 64.3 | 21.28361 | 72.95000 | 0.406 | 0.784 | | | | | | | 4.50 | 0.509 | 69.9 | 7.92 | | |
| Thames | 9.45 | 51.42889 | -0.31722 | 0.0279 | 0.0647 | | | | | | | 0.309 | 0.0350 | 32.8 | 3.71 | | |
| Vistula | 194 | 54.25639 | 18.94639 | 1.20 | 19.8 | 0.670 | 0.180 | | 15.9 | | 81.9 | 13.3 | 1.51 | 68.7 | 7.79 | | 0.0951 |
| Xijiang | 359 | 23.06917 | 112.45000 | 0.961 | 1.99 | 0.970 | 0.020 | | 2.47 | | 6.90 | 10.6 | 1.21 | 29.7 | 3.36 | | 0.487 |
| Yenisey | 2489 | 67.44667 | 86.50194 | 18.0 | 219 | 0.880 | 0.040 | 39.8 | 19.2 | 16.0 | 7.70 | 200 | 22.6 | 80.3 | 9.10 | 1.00 | 1.00 |
| Yukon | 818 | 61.93444 | -162.88056 | 0.383 | 23.9 | 0.920 | 0.070 | 28.6 | 19.8 | 35.0 | 24.2 | 4.24 | 0.481 | 5.19 | 0.588 | 0.148 | 0.0242 |

*Molar discharge is calculated based on chemical composition and substate density similar to upper continental crust presented in Table2

Table 2. Assumed and optimized model parameter values

| Variable | Symbol | Value | Units | References |
|---|---|---|---|---|
| ***Assumed values*** | | | | |
| Molar concentration in bedrock | | | | Rudnick & Gao (2003), Hren et al. (2007), White & Brantley (2003) |
| Si, Quartz | $R_{Si,qz}N_{qz}$ | 11971 | mol $m^{-3}$ | |
| Si, non-quartz | $R_{Si,nqz}N_{nqz}$ | 17957 | mol $m^{-3}$ | |
| SCM, non-quartz | $R_{SCM,nqz}N_{nqz}$ | 3390 | mol $m^{-3}$ | |
| Sequestration factor | $\sigma$ | 1.50 | | Kim et al. (2014, 2017) |
| Substrate density | $\rho$ | 2700 | kg $m^{-3}$ | |
| Soil thickness | $^{soil}h$ | 1.00 | m | Arvin et al. (2017) |
| ***Optimized values*** | | | | |
| Reaction rate for rock (quartz) | $^{rock}K_{qz}$ | 0.00 | $s^{-1}$ | This study |
| Reaction rate for rock (non-quartz) | $^{rock}K_{nqz}$ | $1.94 \times 10^{-13}$ | $s^{-1}$ | This study |
| Ratio of dust to rock reaction rate | $S^*$ | 108 | | This study |
| Ratio of saprolite to soil thickness | $z^*$ | $8.62 \times 10^{-15}$ | | This study |

Table 3. Input and output fluxes from weathering model

| River | Watershed Area ($10^9$ m$^2$) | River Chemistry | | | | Dust Deposition | |
|---|---|---|---|---|---|---|---|
| | | Flux | | Chemical Weathering Rate | Physical Weathering Rate | Modern | LGM |
| | | Si ($10^{-3}$ mol m$^{-2}$ yr$^{-1}$) | SCM ($10^{-3}$ mol m$^{-2}$ yr$^{-1}$) | ($10^{-3}$ kg m$^{-2}$ yr$^{-1}$) | ($10^{-3}$ kg m$^{-2}$ yr$^{-1}$) | ($10^{-3}$ kg m$^{-2}$ yr$^{-1}$) | ($10^{-3}$ kg m$^{-2}$ yr$^{-1}$) |
| Amazon | 4689 | 89.2 | 40.6 | 46.9 | 196 | 4.86 | 7.23 |
| Columbia | 625 | 38.9 | 22.4 | 40.6 | 22.5 | 2.26 | 4.56 |
| Congo | 3623 | 27.4 | 13.3 | 11.5 | 6.16 | 8.06 | 12.7 |
| Ebro | 12.1 | 15.5 | 151 | 95.6 | 186 | 6.44 | 7.64 |
| Kolyma* | 536 | 13.0 | 9.34 | 14.7 | 25.2 | 1.11 | 145 |
| Limpopo | 201 | 0.424 | 1.36 | 14.0 | 74.9 | 1.98 | 2.65 |
| Mackenzie* | 1643 | 9.36 | 13.6 | 35.9 | 23.1 | 0.364 | 2.77 |
| Mekong | 763 | 7.47 | 5.98 | 58.1 | 189 | 1.44 | 2.03 |
| Mississippi* | 2928 | 27.8 | 17.7 | 49.1 | 153 | 11.8 | 231 |
| N. Dvina* | 315 | 16.8 | 61.0 | 56.2 | 13.6 | 5.96 | 31.2 |
| Neva | 232 | 1.09 | 16.7 | 19.1 | 2.96 | 4.37 | 25.1 |
| Orinoco | 818 | 66.1 | 20.8 | 25.6 | 136 | 4.54 | 6.45 |
| Po* | 1.69 | 83.4 | 21.6 | 247 | 231 | 11.7 | 30.6 |
| Rhone | 10.2 | 33.8 | 22.3 | 192 | 292 | 10.5 | 19.5 |

* Basins likely partially glaciated during LGM

Table 3. Input and output fluxes from weathering model (continued)

| River | Weathering Model | | | | | | | | | | |
|---|---|---|---|---|---|---|---|---|---|---|---|
| | Modern | | | | | LGM | | | | | |
| | Si | | SCM | | Fraction from Dust | Si | | SCM | | Fraction from Dust | LGM Flux Enhancement |
| | Flux ($10^{-3}$ mol $m^{-2}$ $yr^{-1}$) | Discharge ($10^{9}$ mol $yr^{-1}$) | Flux ($10^{-3}$ mol $m^{-2}$ $yr^{-1}$) | Discharge ($10^{9}$ mol $yr^{-1}$) | | Flux ($10^{-3}$ mol $m^{-2}$ $yr^{-1}$) | Discharge ($10^{9}$ mol $yr^{-1}$) | Flux ($10^{-3}$ mol $m^{-2}$ $yr^{-1}$) | Discharge ($10^{9}$ mol $yr^{-1}$) | | |
| Amazon | 66.8 | 313 | 18.9 | 88.6 | 26.6% | 74.8 | 351 | 21.2 | 99.3 | 26.6% | 12.0% |
| Columbia | 29.5 | 18.4 | 8.36 | 5.22 | 30.3% | 38.7 | 24.2 | 10.9 | 6.84 | 30.3% | 31.0% |
| Congo | 57.3 | 208 | 16.2 | 58.8 | 61.8% | 77.9 | 282 | 22.1 | 79.9 | 61.8% | 35.8% |
| Ebro | 55.8 | 0.677 | 15.8 | 0.192 | 38.4% | 59.9 | 0.726 | 17.0 | 0.206 | 38.4% | 7.22% |
| Kolyma* | 22.9 | 12.3 | 6.48 | 3.47 | 19.9% | 616 | 330 | 174 | 93.4 | 19.9% | 2590% |
| Limpopo | 6.92 | 1.39 | 1.96 | 0.395 | 58.2% | 8.32 | 1.67 | 2.35 | 0.474 | 58.2% | 20.1% |
| Mackenzie* | 21.5 | 35.3 | 6.09 | 10.0 | 6.77% | 31.1 | 51.1 | 8.81 | 14.5 | 6.8% | 44.6% |
| Mekong | 35.4 | 27.1 | 10.0 | 7.66 | 13.8% | 37.4 | 28.6 | 10.6 | 8.09 | 13.8% | 5.57% |
| Mississippi* | 59.2 | 173 | 16.8 | 49.1 | 59.2% | 781 | 2288 | 221 | 648 | 59.2% | 1221% |
| N. Dvina* | 48.9 | 15.4 | 13.8 | 4.36 | 49.4% | 148 | 46.5 | 41.8 | 13.2 | 49.5% | 202% |
| Neva | 40.3 | 9.36 | 11.4 | 2.65 | 46.9% | 130 | 30.1 | 36.8 | 8.54 | 46.9% | 222% |
| Orinoco | 56.8 | 46.4 | 16.1 | 13.1 | 30.4% | 63.9 | 52.3 | 18.1 | 14.8 | 30.4% | 12.6% |
| Po* | 75.3 | 0.127 | 21.3 | 0.0359 | 46.6% | 132 | 0.223 | 37.4 | 0.0630 | 46.6% | 75.5% |
| Rhone | 69.1 | 0.703 | 19.6 | 0.199 | 44.4% | 95.4 | 0.970 | 27.0 | 0.275 | 44.4% | 38.0% |

* Basins likely partially glaciated during LGM

# Figures

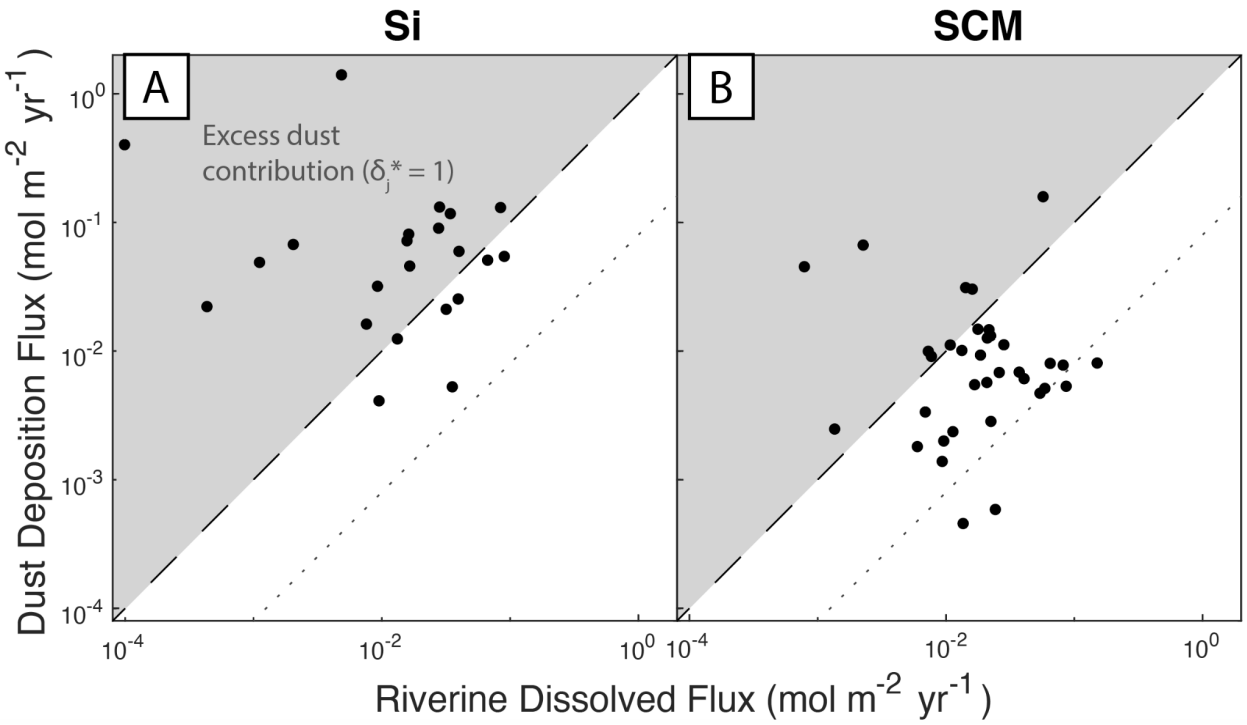


Figure 1: Observed riverine dissolved ion, and corresponding modeled dust deposition flux for A) Si and B) silicate-derived Ca + Mg (SCM) from our mass balance analysis in Section 2. The dashed line represents a 1:1 correspondence ($\delta_j$* = 1), while the dotted line represents a 0.1:1 correspondence ($\delta_j$* = 0.1). A substantial fraction of the observed Si and SCM flux in rivers could be explained by dust inputs.

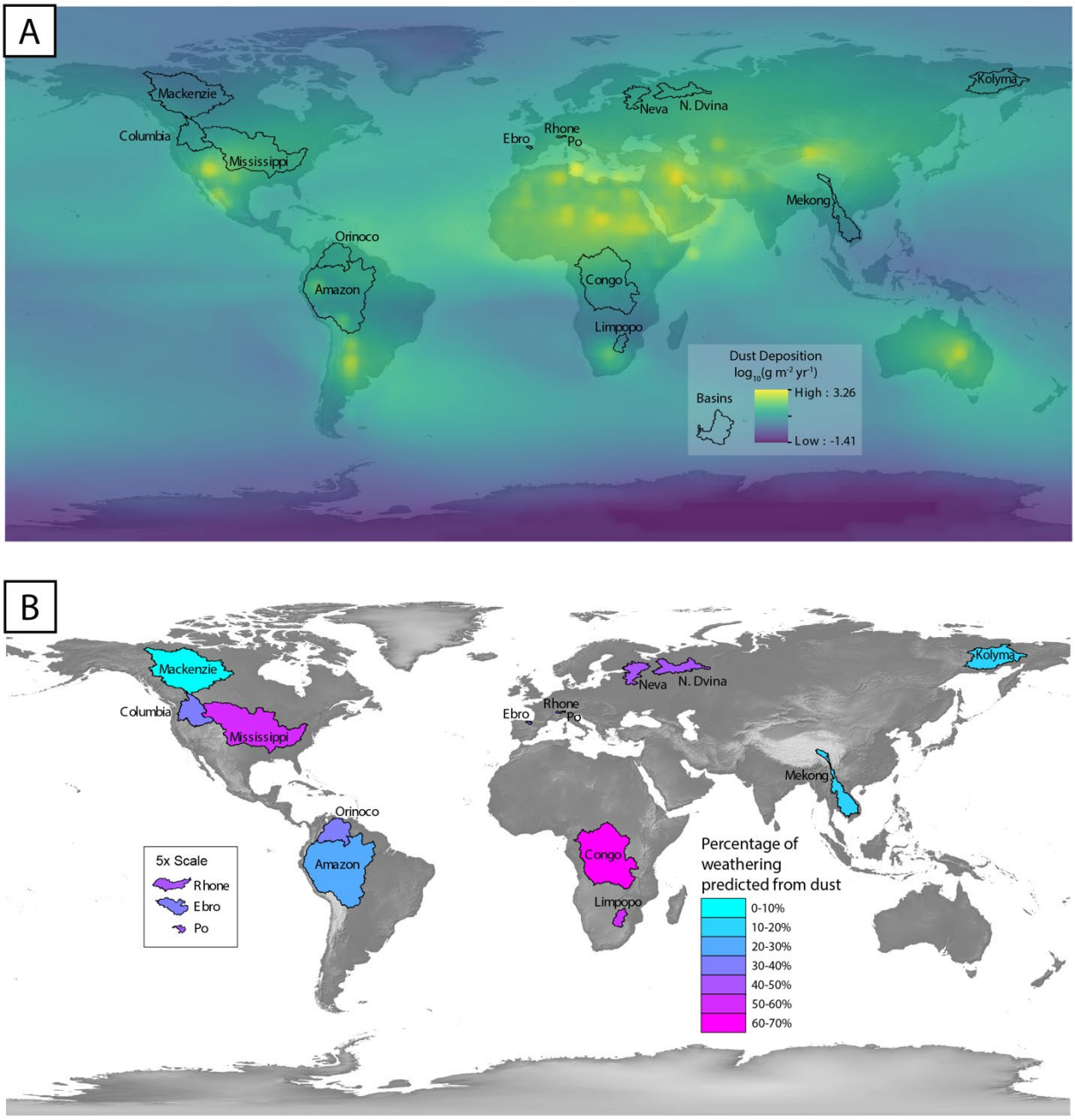


Figure 2: (A) Global modern dust flux from Mahowald et al. (2006) in $\log_{10}$(g $m^{-2}$ $yr^{-1}$) at 1 $km^2$ resolution with sampled basin boundaries, as well as (B) dust-derived proportion of solute fluxes for both Si and SCM and for each basin according to our steady-state weathering model (Section 3). We observe that dust-derived weathering flux in every basin except the Mackenzie is predicted to comprise > 10% of total silicate weathering flux.

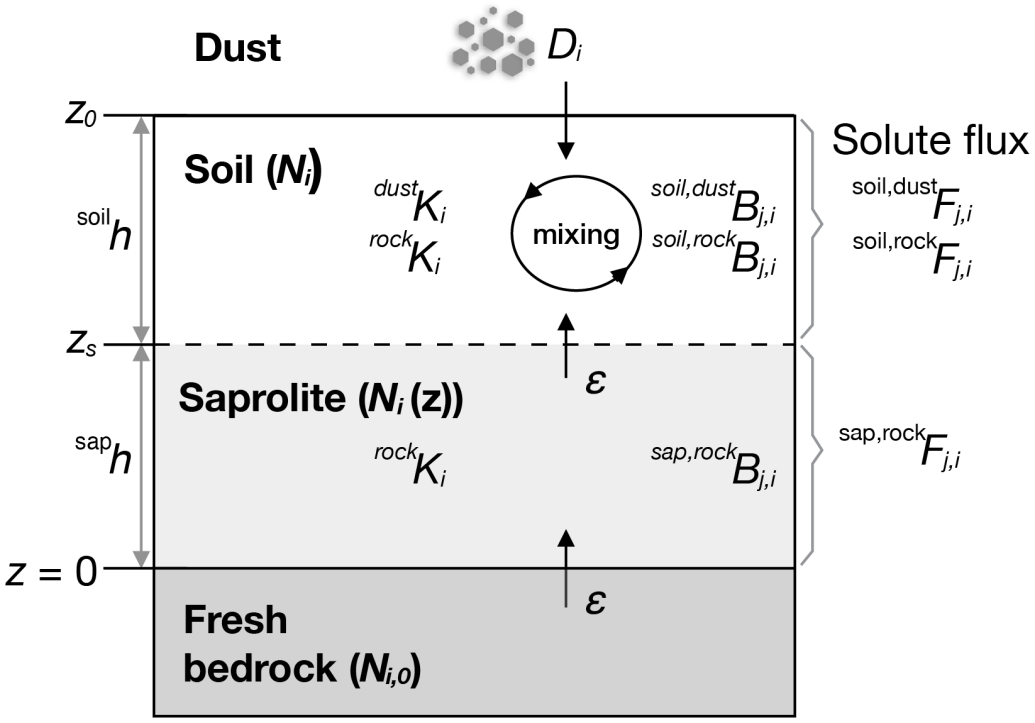


Figure 3: Conceptual framework of the steady-state weathering model. Three subsurface weathering zones, including fresh bedrock, saprolite, and soil, are shown with corresponding variables for their vertical position ($z$), thickness ($h$), material concentration ($N_i$), reaction rate ($^{rock}K_i$), solute production rate ($B_{j,i}$), and solute flux ($F_{j,i}$) for mineral phase $I$ and solute phase $j$. $\varepsilon$ indicates erosion rate, which equals the velocity of rock supply to the weathering zone. $D_i$ is the dust input flux to soil. Variables are fully explained in Methods and Appendix B.

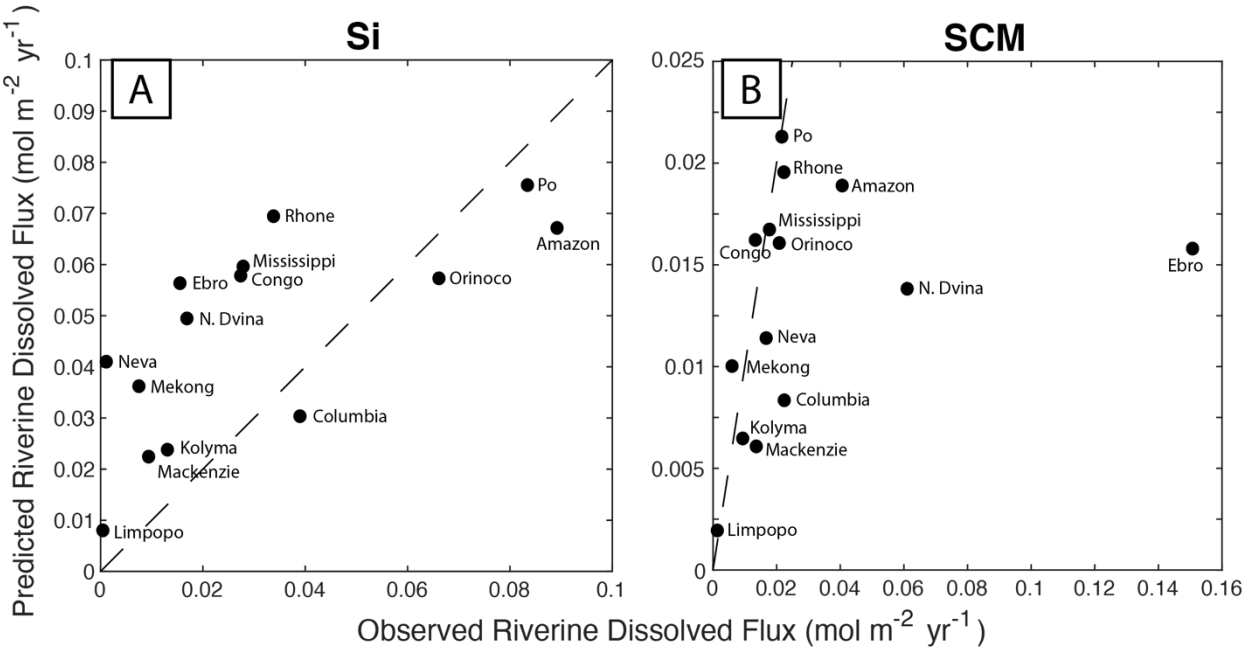


Figure 4: Observed and model-predicted riverine flux for A) Si and B) silicate-derived Ca + Mg (SCM). Vertical axis values for each plot represent best-fitting predicted values based on the steady-state weathering model described in the text. The dashed line shows 1:1 correspondence.

# Supplemental Material

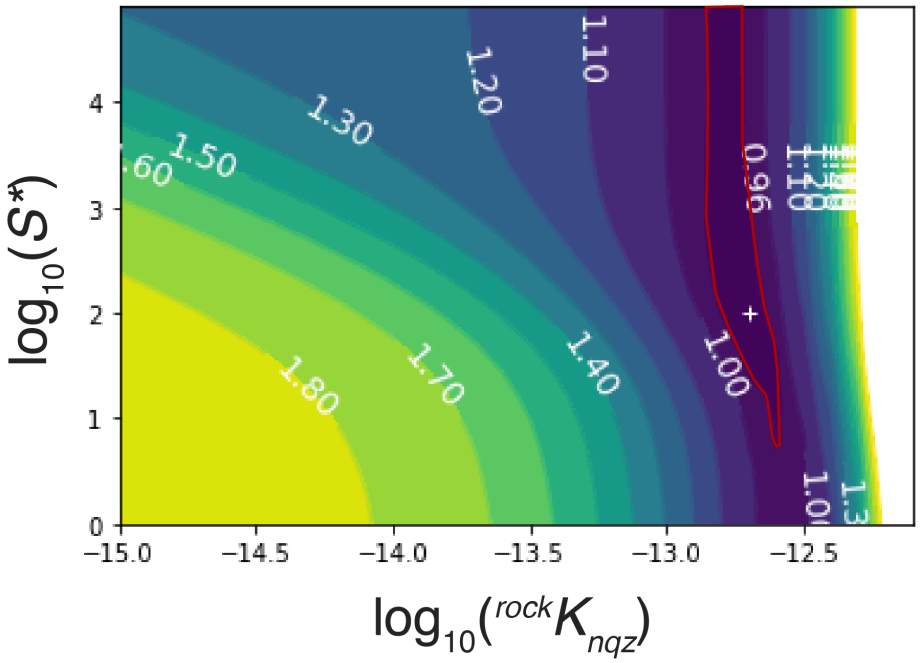


Figure A1: Plot demonstrating the normalized error space, calculated as misfit error normalized by the data variance, for varying ranges of ${}^{rock}K_{nqz}$ and $S^*$. The optimized ${}^{rock}K_{nqz}$ and $S^*$ with the minimal misfit error normalized by the data variance (0.940) is shown with a plus symbol. A narrow range of ${}^{rock}K_{nqz}$ (~$10^{-12.6}$ – $10^{-12.8}$ $s^{-1}$) outlined in red tends to have low misfit normalized error (< 0.96).

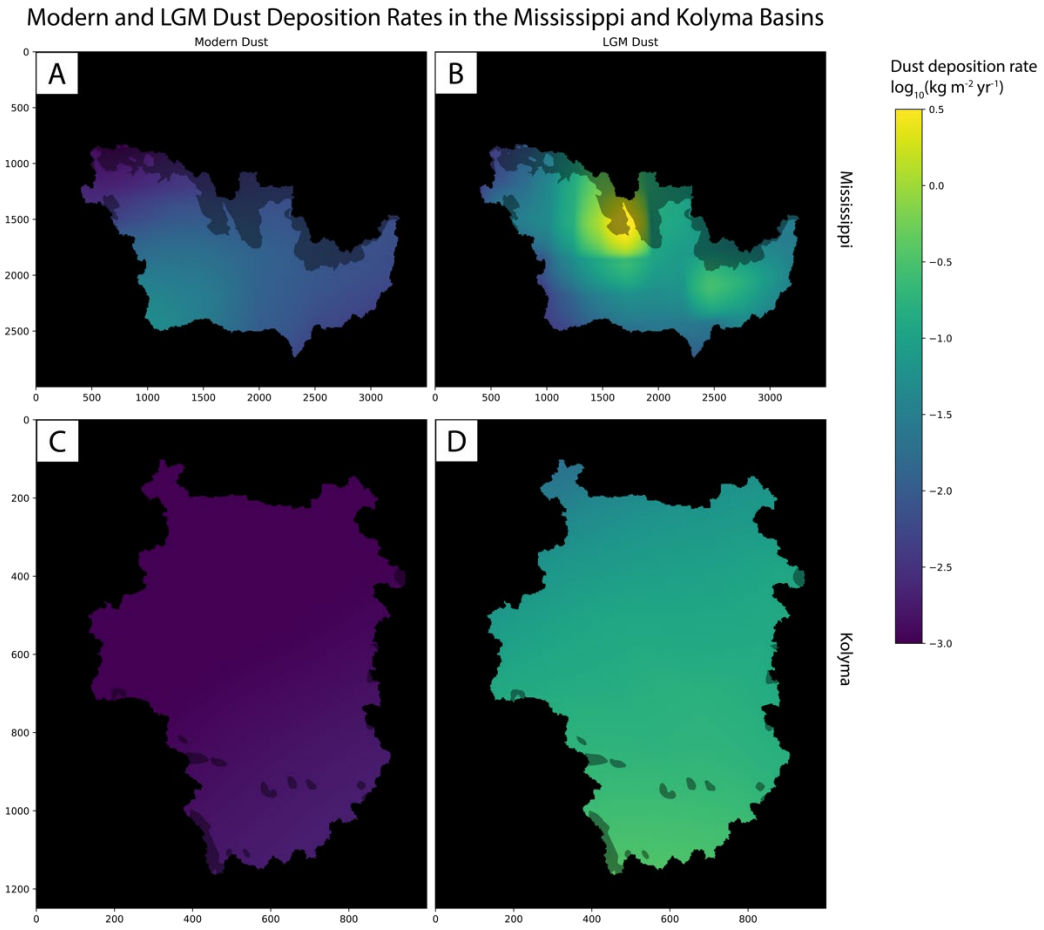


Figure A2: Maps of dust flux distributions in $\log_{10}$(kg $m^{-2}$ $yr^{-1}$) for modern (A, C) and LGM (B, D) cases in the Mississippi basin (A, B) and the Kolyma basin (C, D). In the Mississippi basin during the LGM (B), one region appears to contribute a high amount of the total basin dust flux, which likely leads to an observed basin-wide elevated LGM dust flux. Dark-shaded regions within each basin indicate LGM glaciation (Batchelor et al., 2019). Due to glaciation and cold periglacial conditions which we expect to lead to decreased weathering rates, weathering rates in these basins are likely overestimated during the LGM.

# References

Aarons, S.M., Arvin, L.J., Aciego, S.M., Riebe, C.S., Johnson, K.R., Blakowski, M.A., Koornneef, J.M., Hart, S.C., Barnes, M.E., Dove, N., Botthoff, J.K., Maltz, M., Aronson, E.L., 2019. Competing droughts affect dust delivery to Sierra Nevada. Aeolian Res. 41. https://doi.org/10.1016/j.aeolia.2019.100545

Abatzoglou, J.T., Dobrowski, S.Z., Parks, S.A., Hegewisch, K.C., 2018. TerraClimate, a high-resolution global dataset of monthly climate and climatic water balance from 1958-2015. Sci. Data 5, 1–12. https://doi.org/10.1038/sdata.2017.191

Aciego, S.M., Riebe, C.S., Hart, S.C., Blakowski, M.A., Carey, C.J., Aarons, S.M., Dove, N.C., Botthoff, J.K., Sims, K.W.W., Aronson, E.L., 2017. Dust outpaces bedrock in nutrient supply to montane forest ecosystems. Nat. Commun. 8. https://doi.org/10.1038/ncomms14800

Aleinikoff, J.N., Muhs, D.R., Sauer, R.R., Fanning, C.M., 1999. Late Quaternary loess in northeastern Colorado: Part II - Pb isotopic evidence for the variability of loess sources. Bull. Geol. Soc. Am. 111, 1876–1883. https://doi.org/10.1130/0016-7606(1999)111<1876:LQLINC>2.3.CO;2

Arvin, L.J., Riebe, C.S., Aciego, S.M., Blakowski, M.A., 2017. Global patterns of dust and bedrock nutrient supply to montane ecosystems. Sci. Adv. 3, 1–11. https://doi.org/10.1126/sciadv.aao1588

Batchelor, C.L., Margold, M., Krapp, M., Murton, D.K., Dalton, A.S., Gibbard, P.L., Stokes, C.R., Murton, J.B., Manica, A., 2019. The configuration of Northern Hemisphere ice sheets through the Quaternary. Nat. Commun. 10, 1–10. https://doi.org/10.1038/s41467-019-11601-2

Bickle, M.J., Chapman, H.J., Tipper, E., Galy, A., De La Rocha, C.L., Ahmad, T., 2018. Chemical weathering outputs from the flood plain of the Ganga. Geochim. Cosmochim. Acta 225, 146–175. https://doi.org/10.1016/j.gca.2018.01.003

Brantley, S.L., Kubicki, J.D., White, A.F., 2008. Kinetics of Water-Rock Interaction. Springer.

Clow, D.W., Drever, J.I., 1996. Weathering rates as a function of flow through an alpine soil. Chem. Geol. 132, 131–141. https://doi.org/10.1016/s0009-2541(96)00048-4

Dixon, J.L., Heimsath, A.M., Amundson, R., 2009. The critical role of climate and saprolite weathering in landscape evolution. Earth Surf. Process. Landforms 34, 613–628. https://doi.org/10.1002/esp

Ferrier, K.L., Kirchner, J.W., 2008. Effects of physical erosion on chemical denudation rates: A numerical modeling study of soil-mantled hillslopes. Earth Planet. Sci. Lett. 272, 591–599. https://doi.org/10.1016/j.epsl.2008.05.024

Ferrier, K.L., Riebe, C.S., Hahm, W.J., 2016. Testing for supply-limited and kinetic-limited chemical erosion in field measurements of regolith production and chemical depletion: Testing limits on chemical erosion rates. Geochem. Geophys. Geosyst. 17, 2270–2285. https://doi.org/10.1002/2016GC006273

G.E.M.S./Water, 2011. United Nations Environment Programme Global Environmental Monitoring System (GEMS)/Water Programme.

Gaillardet, J., Dupré, B., Louvat, P., Allègre, C.J., 1999. Global silicate weathering and $CO_2$ consumption rates deduced from the chemistry of large rivers. Chem. Geol. 159, 3–30. https://doi.org/10.1016/S0009-2541(99)00031-5

Goddéris, Y., François, L.M., Probst, A., Schott, J., Moncoulon, D., Labat, D., Viville, D., 2006.

Modelling weathering processes at the catchment scale: The WITCH numerical model. Geochim. Cosmochim. Acta 70, 1128–1147. https://doi.org/10.1016/j.gca.2005.11.018

Goddéris, Y., Williams, J.Z., Schott, J., Pollard, D., Brantley, S.L., 2010. Time evolution of the mineralogical composition of Mississippi Valley loess over the last 10kyr: Climate and geochemical modeling. Geochim. Cosmochim. Acta 74, 6357–6374. https://doi.org/10.1016/j.gca.2010.08.023

H.Y.B.A.M., 2013. Geodynamical, hydrological and biogeochemical control of erosion/alteration and material transport in the Amazon basin.

Hartmann, J., Moosdorf, N., 2012. The new global lithological map database GLiM: A representation of rock properties at the Earth surface. Geochem. Geophys. Geosyst. 13, 1–37. https://doi.org/10.1029/2012GC004370

Hilley, G.E., Chamberlain, C.P., Moon, S., Porder, S., Willett, S.D., 2010. Competition between erosion and reaction kinetics in controlling silicate-weathering rates. Earth Planet. Sci. Lett. 293, 191–199. https://doi.org/10.1016/j.epsl.2010.01.008

Hilley, G.E., Porder, S., 2008. A framework for predicting global silicate weathering and $CO_2$ drawdown rates over geologic time-scales. Proc. Natl. Acad. Sci. 105, 16855–16859. https://doi.org/10.1073/pnas.0801462105

Hren, M.T., Hilley, G.E., Chamberlain, C.P., 2007. The relationship between tectonic uplift and chemical weathering rates in the Washington Cascades: Field measurements and model predictions. Am. J. Sci. 307, 1041–1063. https://doi.org/10.2475/09.2007.01

Jacobson, A.D., Blum, J.D., Chamberlain, C.P., Poage, M.A., Sloan, V.F., 2002. Ca/Sr and Sr isotope systematics of a Himalayan glacial chronosequence: Carbonate versus silicate

weathering rates as a function of landscape surface age. Geochim. Cosmochim. Acta 66, 13–27. https://doi.org/10.1016/S0016-7037(01)00755-4

Kim, H., Bishop, J.K.B., Dietrich, W.E., Fung, I.Y., 2014. Process dominance shift in solute chemistry as revealed by long-term high-frequency water chemistry observations of groundwater flowing through weathered argillite underlying a steep forested hillslope. Geochim. Cosmochim. Acta 140, 1–19. https://doi.org/10.1016/j.gca.2014.05.011

Kim, H., Dietrich, W.E., Thurnhoffer, B.M., Bishop, J.K.B., Fung, I.Y., 2017. Controls on solute concentration-discharge relationships revealed by simultaneous hydrochemistry observations of hillslope runoff and stream flow: The importance of critical zone structure. Water Resour. Res. 53, 1424–1443. https://doi.org/10.1002/2016WR019722

Kurtz, A.C., Derry, L.A., Chadwick, O.A., 2001. Accretion of Asian dust to Hawaiian soils: Isotopic, elemental, and mineral mass balances. Geochim. Cosmochim. Acta 65, 1971–1983. https://doi.org/10.1016/S0016-7037(01)00575-0

Lawrence, C.R., Neff, J.C., 2009. The contemporary physical and chemical flux of aeolian dust: A synthesis of direct measurements of dust deposition. Chem. Geol. 267, 46–63. https://doi.org/10.1016/j.chemgeo.2009.02.005

Lehner, B., Verdin, K., Jarvis, A., 2008. New global hydrography derived from spaceborne elevation data. Eos (Washington. DC). 89, 93–94. https://doi.org/10.1029/2008EO100001

Macdonald, F.A., Swanson-Hysell, N.L., Park, Y., Lisiecki, L., Jagoutz, O., 2019. Arc-continent collisions in the tropics set Earth's climate state. Science 364, 181–184. https://doi.org/10.1126/science.aav5300

Mahowald, N.M., Baker, A.R., Bergametti, G., Brooks, N., Duce, R.A., Jickells, T.D., Kubilay, N.,

Prospero, J.M., Tegen, I., 2005. Atmospheric global dust cycle and iron inputs to the ocean. Global Biogeochem. Cycles 19. https://doi.org/10.1029/2004GB002402

Mahowald, N.M., Muhs, D.R., Levis, S., Rasch, P.J., Yoshioka, M., Zender, C.S., Luo, C., 2006. Change in atmospheric mineral aerosols in response to climate: Last glacial period, preindustrial, modern, and doubled carbon dioxide climates. J. Geophys. Res. Atmos. 111. https://doi.org/10.1029/2005JD006653

Mahowald, N., Albani, S., Kok, J.F., Engelstaeder, S., Scanza, R., Ward, D.S., Flanner, M.G., 2014. The size distribution of desert dust aerosols and its impact on the Earth system. Aeolian Res. 15, 53–71. https://doi.org/10.1016/j.aeolia.2013.09.002

Marcotte, A.R., Anbar, A.D., Majestic, B.J., Herckes, P., 2020. Mineral Dust and Iron Solubility: Effects of Composition, Particle Size, and Surface Area. Atmosphere 11. https://doi.org/10.3390/atmos11050533

McIntosh, J.C., Schaumberg, C., Perdrial, J., Harpold, A., Vázquez-Ortega, A., Rasmussen, C., Vinson, D., Zapata-Rios, X., Brooks, P.D., Meixner, T., Pelletier, J., Derry, L., Chorover, J., 2017. Geochemical evolution of the Critical Zone across variable time scales informs concentration-discharge relationships: Jemez River Basin Critical Zone Observatory. Water Resour. Res. 53, 4169–4196. https://doi.org/10.1029/eo064i046p00929-04

Moon, S., Chamberlain, C.P., Hilley, G.E., 2014. New estimates of silicate weathering rates and their uncertainties in global rivers. Geochim. Cosmochim. Acta 134, 257–274. https://doi.org/https://doi.org/10.1016/j.gca.2014.02.033

Nelder, J.A., Mead, R., 1965. A simplex method for function minimization". Comput. J. 7, 308–313.

Pelletier, J.D., Broxton, P.D., Hazenberg, P., Zeng, X., Troch, P.A., Niu, G.-Y., Williams, Z., Brunke, M.A., Gochis, D., 2015. A gridded global data set of soil, intact regolith, and sedimentary deposit thicknesses for regional and global land surface modeling. J. Adv. Model. Earth Syst. 8, 41–65. https://doi.org/10.1002/2015MS000526

Pett-Ridge, J.C., Derry, L.A., Barrows, J.K., 2009. Ca/Sr and 87Sr/86Sr ratios as tracers of Ca and Sr cycling in the Rio Icacos watershed, Luquillo Mountains, Puerto Rico. Chem. Geol. 267, 32–45. https://doi.org/10.1016/j.chemgeo.2008.11.022

Porder, S., Clark, D.A., Vitousek, P.M., 2006. Persistence of rock-derived nutrients in the wet tropical forests of La Selva, Costa Rica. Ecology 87, 594–602. https://doi.org/10.1890/05-0394

Raymo, M.E., Ruddiman, W.F., 1992. Tectonic forcing of late Cenozoic climate. Nature 359, 117–122. https://doi.org/10.1038/359117a0

Ridgwell, A.J., Kohfeld, K.E., 2002. Dust in the Earth System: The Biogeochemical Linking of Land, Air, and Sea. Adv. Earth Sci. 51–68, 2905–2924. https://doi.org/10.1098/rsta.2002.1096

Ridgwell, A.J., Watson, A.J., 2002. Feedback between aeolian dust, climate and atmospheric $CO_2$ in glacial time. Paleoceanography 17. https://doi.org/10.1029/2001pa000729

Riebe, C.S., Kirchner, J.W., Finkel, R.C., 2004. Erosional and climatic effects on long-term chemical weathering rates in granitic landscapes spanning diverse climate regimes. Earth Planet. Sci. Lett. 224, 547–562. https://doi.org/10.1016/j.epsl.2004.05.019

Roberts, H.M., Muhs, D.R., Wintle, A.G., Duller, G.A.T., Bettis, E.A., 2003. Unprecedented last-glacial mass accumulation rates determined by luminescence dating of loess from western

Nebraska. Quat. Res. 59, 411–419. https://doi.org/10.1016/S0033-5894(03)00040-1

Rudnick, R.L., Gao, S., 2013. Composition of the Continental Crust, 2nd ed, Treatise on Geochemistry: Second Edition. Elsevier Ltd. https://doi.org/10.1016/B978-0-08-095975-7.00301-6

Schulz, M.S., White, A.F., 1999. Chemical weathering in a tropical watershed, Luquillo Mountains, Puerto Rico III: Quartz dissolution rates. Geochim. Cosmochim. Acta 63, 337–350. https://doi.org/10.1016/S0016-7037(99)00056-3

Simonson, R.W., 1995. Airborne dust and its significance to soils. Geoderma 65, 1–43. https://doi.org/10.1016/0016-7061(94)00031-5

Tanaka, T.Y., Chiba, M., 2006. A numerical study of the contributions of dust source regions to the global dust budget. Glob. Planet. Change 52, 88–104. https://doi.org/10.1016/j.gloplacha.2006.02.002

Taylor, S.R., McLennan, S.M., 1985. The Continental Crust: Its Composition and Evolution. Blackwell Scientific Publications. Oxford.

Torres, M.A., Moosdorf, N., Hartmann, J., Adkins, J.F., West, A.J., 2017. Glacial weathering, sulfide oxidation, and global carbon cycle feedbacks. Proc. Natl. Acad. Sci. 114, 8716–8721. https://doi.org/10.1073/pnas.1702953114

Tourtelot, H.A., 1971. Chemical compositions of rock types as factors in our environment. Mem. Geol. Soc. Am. 123, 13–29. https://doi.org/10.1130/MEM123-p13

Udden, J.A., 1914. Mechanical composition of clastic sediments. Geol. Soc. Am. Bull. 25, 655–744. https://doi.org/10.1130/gsab-25-655

Waldbauer, J.R., Page Chamberlain, P.C., 2005. Influence of Uplift, Weathering, and Base Cation

Supply on Past and Future $CO_2$ Levels, in: Baldwin, I.T., Caldwell, M.M., Heldmaier, G., Jackson, R.B., Lange, O.L., Mooney, H.A., Schulze, E.-D., Sommer, U., Ehleringer, J.R., Denise Dearing, M., Cerling, T.E. (Eds.), A History of Atmospheric $CO_2$ and Its Effects on Plants, Animals, and Ecosystems. Springer, New York, pp. 166–184. https://doi.org/10.1007/0-387-27048-5_8

White, A.F., Brantley, S.L., 2003. The effect of time on the weathering of silicate minerals: Why do weathering rates differ in the laboratory and field? Chem. Geol. 202, 479–506. https://doi.org/10.1016/j.chemgeo.2003.03.001

Willmott, C.J., Matsuura, K., 2001. Terrestrial Air Temperature and Precipitation: Monthly and Annual Time Series (1950 - 1999). http://climate.geog.udel.edu/~climate/html_pages/README.ghcn_ts2.html.